The CHIMERE chemistry-transport model v2023r1

Laurent MENUT[1], Arineh CHOLAKIAN[1], Romain PENNEL[1], Guillaume SIOUR[2], Sylvain MAILLER[1], Myrto VALARI[1], Lya LUGON[3], and Yann MEURDESOIF[4]

[1]Laboratoire de Météorologie Dynamique (LMD), Ecole Polytechnique, IPSL Research University, Ecole Normale Supérieure, Université Paris-Saclay, Sorbonne Universités, UPMC Université Paris 06, CNRS, Route de Saclay, 91128 Palaiseau, France
[2]Univ Paris Est Créteil and Université Paris Cité, CNRS, LISA, F-94010 Créteil, France
[3]CEREA, Ecole des Ponts ParisTech, EdF R&D, 77455 Marne-la Vallée, France
[4]Laboratoire des Sciences du Climat et de l'Environnement, IPSL, CEA/CNRS/UVSQ, Gif-sur-Yvette, France

Correspondence: Laurent Menut, menut@lmd.ipsl.fr

Abstract. A new version of the CHIMERE model is presented. This version contains both computational and physico-chemical changes. The computational changes make it easy to choose the variables to be extracted as a result, including values of maximum sub-hourly concentrations. Performance tests show that the model is 1.5 to 2 times faster than the previous version for the same set-up. Processes have been modified and updated such as turbulence, transport schemes and dry deposition.

5   Optimization was also performed for the management of emissions such as anthropogenic and mineral dust. The impact of fires on wind speed, soil properties and LAI was added. Pollen emissions, transport and deposition were added for birch, ragweed, olive, grass. The model is validated with a simulation covering Europe with 60×60 km resolution and the entire year of 2019. Results are compared to various measurements, and statistical scores show that the model provides better results than the previous versions.

10   **1   Introduction**

Chemistry-transport modelling is useful for analysis and forecast of atmospheric pollution events. Regional deterministic models have proven their interest for studies about climate change, emissions regulations, day to day pollution evolution, health effects, among many other topics. These models have to be accurate and efficient, with at the same time a good accuracy and a low computational time.

15   The CHIMERE chemistry-transport model has been under continuous development since 1999. Several versions have been released as open-source software since the first one. The model is now used for analysis and forecast in many institutes, research laboratories and private companies. For the last ten years, releases were distributed with a frequency of a new major one every three years. Version v2014 included, the possibility to read emission fluxes from fires, the SAPRC chemical mechanism, an adaptive time-step and new datasets for the chemical boundary conditions (Menut et al., 2013). Version v2017 (Mailler et al.,

20   2017) added the possibility to use an hemispheric domain, new datasets to calculate mineral dust emissions in any global locations, the addition of the Fast-JX module to calculate photolysis rates and diagnose the lidar profiles and the addition of a new resuspension scheme. Version v2020 provides coupling with the WRF meteorological model through the OASIS3-MCT

external coupler (Craig et al., 2017). In addition, many chemical processes were added in the model: Volatility Basis Set aerosol schemes, DMS emissions and chemistry, the H^2O aerosol scheme, the mineral dust mineralogy, the sub-grid scale variability of anthropogenic emissions and an updated strategy for vertical advection of pollutants, (Menut et al., 2021a).

The novelties in CHIMERE v2023r1 relative to previous model versions concern the physical and chemical processes as well
5 as the technical implementation of the model. In this article, we summarize all new developments and we show examples of their use. The main changes regarding the technical implementation are: (i) new file format and databases for anthropogenic and fires emissions, (ii) addition of the XIOS2 library, (iii) modularization of subroutines, (iv) possibility to output a partial AOD for each aerosol species and (v) a new Fortran90 implementation of the ISORROPIA model. Regarding the physico-chemical processes, the main changes are: (i) new calculation for the turbulence and dry deposition, (ii) new advection schemes, (iii)
10 implementation of pollen emission, (iv) parameterization of the impact of fires on mineral dust emissions and Leaf Area Index, (v) externalisation of the modules included in the SSH-aerosol package.

In this article, we present in details all these novelties. The model structure is detailed and the computing time is illustrated. Test cases are performed and comparisons to observations are presented in order to quantify the model ability to reproduce real pollution events. Finally, a general conclusion about this new version is presented in section 9 including some perspectives for
15 future developments.

2 Model numerical structure

One of the most important changes for this model version is a complete re-organization of the code structure. It could appear as not impacting the users in their daily way to use the model, but in fact, it changes a lot the simulations. The simulation are faster and the implementation of the XIOS (XML-IO-SERVER) library enables to better manage the outputs as well as their
20 size. All these changes are described in this section.

2.1 Modularization

The code was rewritten to have programs organized as Fortran90 modules. This does not change the order of the processes calculations nor that the results of the simulation. It is just an internal choice to have more easily optimizable code for future developments.
25 Figure 1 presents the organization chart of this model version. The main program is called *chimere*. This program mainly manages three different blocks. First, the *inichimere* routine is called and is dedicated to the initialization of each modules : *i.e* reading input parameters (namelists or aerosol size distribution, list of chemical species, among others), computing of fixed parameters, array allocations. Depending on the processes requested by the user, modules are initialized or not, this way we prevent for unecessary file reading or memory burden. In case of online coupling, an additional namelist for OASIS is read.
30 Second, another initialization part has to be done in the *iniworker* routine. This is performed only for the first simulated hour, in order to fill values at time 0 for all input variables: meteorology, turbulence, anthropogenic and fire emissions (depending on input databases) and boundary conditions. Third, the loop over time starts and is managed for each processor in the *worker*
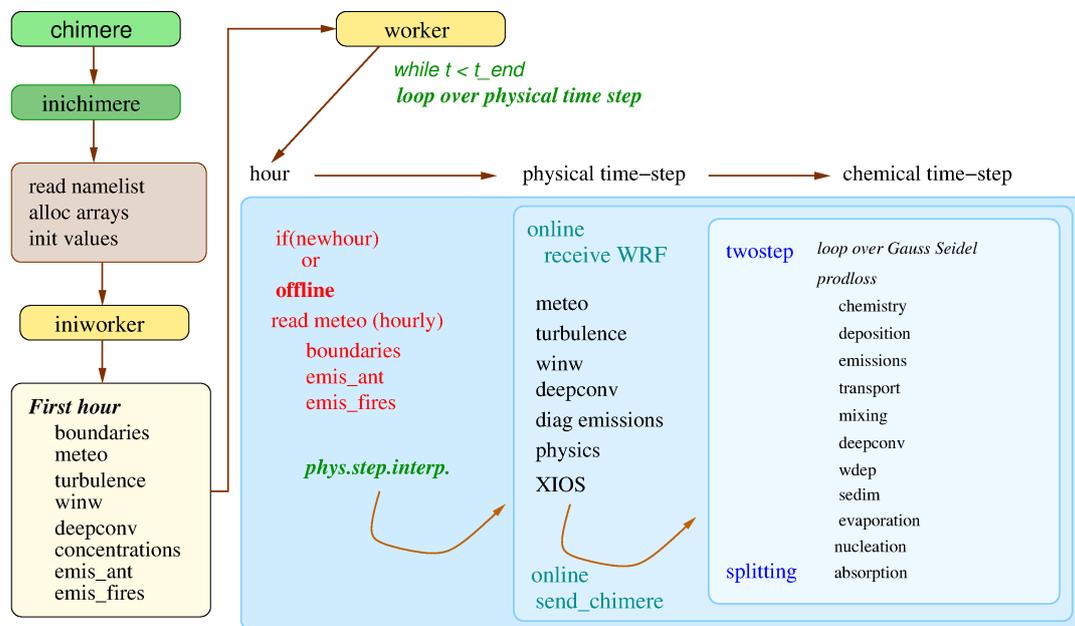
Figure 1. *Organization chart of the CHIMERE v2023r1 version.*

routine. This loop is performed at the physical time-step, a sub-hourly division depending on the domain cells sizes. Depending on the offline (no feedback between chemistry and weather) or online (in blue) simulation, meteorological fields are read (hourly, in red) or received from WRF (physical time-step, in blue). In case of online, the concentrations are send to WRF to take into account direct and indirect effects for the next physical time-step. If offline, if the time-step coincides with an entire
5   hour, the hourly boundary conditions, anthropogenic and fires emissions are updated. For these hourly fields, a linear time interpolation is performed to retrieve information at the corresponding physical time-step. Next, all processes related to the physical time-step are performed: emissions, resuspension, aerosol physics, mixing, photolysis, deposition and chemical rates. Having all necessary information, a loop is performed at the chemical time-step. Two chemical solvers are available: *twostep* and *splitting*, as already explained in Menut et al. (2021a). For example in *twostep*, the first step is performed then an additional
10 loop is performed with Gauss-Seidel iterations for the second step . Finally, the newly implemented XIOS routine is called to write the results on disc.

The model has thus three main steps: initialization for modules, initialization of first tables values at time 0 and time integration. The time integration contains three levels: (i) a sub-hourly physical time-step, depending on the grid size for meteorological variables accuracy mainly, (ii) a chemical time-step depending on the Courant-Friedrichs-Lewy (CFL) condition (Courant
15 et al., 1952) and (iii) Gauss-Seidel iterations (at least two are recommended).

2.2 XIOS I/O management library

XIOS in its version 2 (XIOS2) has been implemented in CHIMERE. XIOS (XML-IO-SERVER) is an open source C++ library dedicated to I/O management usable in conjunction with numerical models written in Fortran/C/C++ (XIOS, 2023). It is a powerful tool for both output history file management as well as spatial and temporal post-processing of data at run time.

5 XIOS was developed with several goals in mind: i) simplifying the I/O management inside the source code by reducing the number of calls needed to send a variable to be written, ii) offering flexibility to the user without having to make modifications inside the source code, iii) making writing and computing happen simultaneously by using asynchronous calls, meaning that the writing will not slow down the computation. XIOS manages to achieve these goals by setting up servers and clients; one or several cpus can be dedicated to XIOS servers which manage I/O processes exclusively. These servers receive asynchronous

10 data from what are called clients (here the chimere ranks) and write them into one or multiple files; they can also manage any additional temporal or spatial post-processing requested by the user. XIOS has been implemented and evaluated in several models. Among many others, IPSL earth system models use XIOS exclusively (Boucher et al., 2020).

File and variable management is done by xml files. For standard use of the model, all necessary files, variables and parameters have been prepared in standard xml files and the use of XIOS is transparent for the user. However, one of the perks of using

15 XIOS is the flexibility it offers the users. This means that the user can create almost any combination of output files they want, adding or removing species or dimensions. Indeed the xml files can be modified or new ones can be created at any time by the user without the need of recompiling the model or in a large part even coding in the model. We list here some common tasks that XIOS can perform:

– Hourly minima, maxima or average of a particular species can be processed by XIOS and written to disk without adding
20 more computation time.

– Species can be written only for a specific part of the domain (like a sounding or a subdomain) or a specific layer (the surface for instance)

– Arithmetic operations can be performed to sum up variables on a chosen dimension

– The user is completely free to define an output file with only the variables that are important for their specific usage

25 Examples for such personalized cases have been provided in the code. It is important to keep in mind that customizing an xml file to create personalized XIOS output files is not limited to the examples provided by the development team and each user can create output files corresponding to their specific needs.

The performance of XIOS compared to the standard I/O system using parallel netcdf4 in the model (called nc4 here after) have been compared extensively. Figure 2 shows runtime comparisons of 30 1-day simulations in different configurations.

30 Two configurations of XIOS have been shown here; the standard configurations that replicates the "nc4" output files to the letter (called "XIOS_full") and an example of a personalized configuration which writes only a list of species necessary for the usage in mind (called "XIOS_slim"). These are compared to the model runtime when it does not write any output, which can
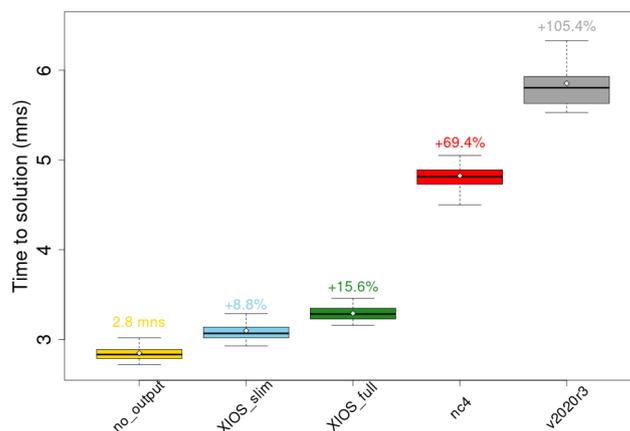
Figure 2. *Runtime comparison of several I/O options implemented in the model. Each boxplot contains 30 × 1-day simulations, black point on each boxplot shows the average for each configuration. Five options are shown - "no_output": Model does not write any output files, "xios_slim": An example of a personalized XIOS output, "xios_full": The standard output files of the model written with XIOS, "nc4": The standard output files of the model written with the standard I/O module in the model and V2020r3, the previous distributed model version. The additional time (in %) is shown above each boxplot. For the "no_output" case the average time (in minutes) is shown.*

be considered as the pure calculation time of the model (including reading of input data). The figure shows that using XIOS offers an important reduction in runtime of the model; adding only 8.8% and 15.6% to the runtime for the "XIOS_slim" and the "XIOS_full" configurations respectively. Compared to the added 69.4% computation time in the case of the standard I/O module, XIOS offers a good performance increase to the model. Finer tuning of the performance is also possible by adapting

5   the number of I/O servers or the size of buffers. Finally, this new model version is compared to the previous one, the distributed v2020r3 version: with a time increase of +105.4%, the new model version is two times faster than the previous one.

2.3   Update of the user parameter namelist

The chimere parameter file *chimere.par* was updated in order to remove some unused parameters and to add novelties. The complete list of parameters is presented in the model documentation (https://www.lmd.polytechnique.fr/chimere/docs/

10   CHIMEREdoc_v2023.pdf) for all possible flags. In this section, only the new flags corresponding to new functionalities are explained.

1. *forecast*: The forecast is re-activated in this model version. It is mainly the way to manage the WRF files when preparing the meteorology.

2. *nproc_chimere*, *nproc_wrf* and *nproc_xios* options are for the management of the simulation as a function of the available

15   processors, for CHIMERE, WRF and XIOS, respectively. Obviously, the total of the three must be less or equal to the total number of the available processors on the user computer. For CHIMERE and WRF, the number of processors

corresponds to the number of subdomains for the parallel computation. If you are 'offline' the number of subdomain are calculated for CHIMERE only.

3. *ifire2dust*, *ifire2lai*, *ifire2drydep*: The effect of the fires on other processes. This takes into account the possible changes of soil erodibility and surface wind speed, the LAI for the biogenic emissions and for the dry deposition of gaseous species following Menut et al. (2023).

4. *ilai*: Select the LAI database, between *ilai*=MOD (Modis, Yuan et al. (2011)), and *ilai*=COP (Copernicus, Fuster et al. (2020)).

5. *ip_ragweed*: Activation of ragweed pollen calculation or not (0). Three schemes are available for this pollen type: (1) for the Sofiev et al. (2013) scheme, (2) for the Efstathiou et al. (2011) and (3) for the Menut et al. (2021b) scheme. Calculations are explained in Section 6.2.

6. *ip_birch*, *ip_grass*, *ip_alder* and *ip_olive* are dedicated to activate (1) or not (0) the pollen emissions for birch, grass, alder and olive, respectively.

7. *ipolresus* activates the resuspension only for pollen.

8. *pollendir* indicates the directory where all pollen databases are stored. For this model version, and having no other available dataset, pollen forcing data are available only over Western Europe.

9. *gtrc* and *ptrc* activate the gaseous and aerosol tracers, respectively. It is necessary to fill in two ascii files (see Section 3.2): *TRACERS_GAS.data* and *TRACERS_PART.data*).

10. *dgrb* is the directory where are stored the global meteorological files in grib format (ECMWF or NCEP).

11. *geodata* is the directory of surface input data for WPS. In this version, WPS (from WRF) is distributed since the domain file used by CHIMERE is the geog file of WRF. This avoid some interpolations of meteorological fields, then reduce errors on the meteorology and speed up the model.

12. *dmin* and *dmax* are the size of the first interval of the first bin and the last interval of the last bin respectively. Values of 0.01 μm and 40 μm are recommended.

13. *iforcut*: if this flag is equal to 1, the calculation of the size distribution is forced to have retained as cut-off diameter of 2.5 and 10 μm.

14. *timeverb*: this flag manages some print on screen providing the time step in each module of the model. It is mainly useful to developers to see if new calculations have an important numerical cost.

15. *AODPerSpecies*: the Aerosol Optical Depth is outputed aerosol species per species.

The chemical module SSH-aerosol (Sartelet et al., 2020) is now compatible with CHIMERE to represent aerosol dynamics. SSH-aerosol is distributed independently of the CHIMERE model and it will evolve on its side in the next few years. It means in order to be able to use this specific option, the user needs to download the SSH-adrosol module and compile it independently of all CHIMERE programs. For this, a specific script is available in CHIMERE main folder to download SSH-aerosol. In the CHIMERE namelist, the use of SSH-aerosol is activated for *soatyp*=h2o or h2or. A specific namelist for SSH-aerosol is

5   proposed in *namelist_ssh* folder, and it can be adapted by the user according to the level of complexity suitable to compute aerosol dynamics. Note that, in this version, the SSH-aerosol package is currently compatible only with the *operator splitting option* and not with the *twostep* option. For consistency between the SOA compounds in gas and particle phases, the Melchior 2 chemical mechanism is recommended.

3 New calculations for the transport

10   ### 3.1 Changes in the advection formulation

New advection schemes have been introduced recently in the CHIMERE model.

First, as described in Lachatre et al. (2020), the Després and Lagoutière (1999) advection scheme has been implemented in the vertical direction. Also described in Lachatre et al. (2020), two options are now available for the representation of vertical velocity: either diagnose it from the horizontal wind components, as it was historically done in CHIMERE, or use

15   the vertical wind speed provided by the meteorological model. These new features were already present in v2020r1 (Menut et al., 2021a). The recent study of Lachatre et al. (2022) has shown that reducing numerical diffusion by using the Després and Lagoutière (1999) advection scheme and using the vertical wind speed w from the meteorological model (*is_diagwinw* = .false. in *chimere.par*) not only reduces vertical diffusion (as already shown in Lachatre et al. (2020)), but also modifies the chemical processes in thin plumes: due to the nonlinearity of tropospheric chemistry, diluting a plume over a larger volume

20   changes not only its distribution, but also the kinetics and relative importance of the chemical processes, as shown in Lachatre et al. (2022) for the case of sulphur oxidation paths in a volcanic plume.

Between CHIMERE versions v2020r1 and v2023r1, four modifications have been brought to horizontal advection:

– the Walcek (2000) advection scheme has been implemented

– the implementation of the PPM scheme (Colella and Woodward (1984)) has been revised and is now faster than the
25   previous implementation.

– the Walcek (2000) advection scheme has been implemented

– the PPM+W advection scheme has been implemented (Mailler et al., 2023c).

Therefore, five horizontal advection schemes are available in chimere2023r1:

– the simple first-order advection scheme of Godunov and Bohachevsky (1959) (too diffusive for practical use)

- the classical second-order scheme of Van Leer (1977)

- the second-order Walcek (2000) advection scheme

- the formally third-order PPM scheme Colella and Woodward (1984).

5   – the formally third-order PPM+W scheme described in Mailler et al. (2023c).

In an academic framework, Mailler et al. (2023c) have shown that the PPM+W performs best among these schemes in terms of accuracy, while the Van Leer and Walcek schemes are computationnally cheaper. The PPM+W scheme has a computational cost similar to PPM.

3.2   Changes in tracer management

10 Introduction of "tracer" emissions inside model simulations including or not other (realistic) emissions is a possibility offered by the CHIMERE model. In CHIMERE, the word "tracer" does not necessarily imply that the species is inert chemically. The emitted species can either be chemically inert (as in Lachatre et al. (2020)) or active (as in Lachatre et al. (2022)), as soon as the emission occurs over a finite number of horizontal points (but possibly spread in the z direction). The user can specify the vertical repartition of tracer emissions, and their evolution in time. This framework is well suited to include emissions due to

15 volcanic eruptions or industrial accidents for example (e.g. Lachatre et al. (2022)), but also to study the behaviour and motion of air masses to and from key areas such as cities or mountain valleys (Lapere et al., 2023; Deroubaix et al., 2019). Lachatre et al. (2022) shows an example of a real species (SO_2) emitted as a tracer over a specific point, along with its normal surfacic anthropogenic emissions from *emisurf*.

In the new version of the CHIMERE model, gas and/or particulate tracers are set in two distinct input files (*TRAC-*
20 *ERS_GAS.data* and *TRACERS_PART.data*). The users decides to activate gas tracers or not by acting on two distinct parameters in the *chimere.par* file:

- *gtrc* : to be set to 1 (resp. 0) to activate (resp. desactivate) gas tracers

- *ptrc* : to be set to 1 (resp. 0) to activate (resp. desactivate) particulate tracers

Compared to earlier model versions, the new model version permits more flexibility and user control for particulate tracer
25 emissions: for each tracer emission event, up to three different emission modes can be specified (from the median diameter and the multiplicative spread of the log-normal distribution), independantly from the modes defined for anthropogenic emissions. In the *TRACERS_PART.data*, for each tracer emission, the user can define the following parameters:

- Longitude and latitude of the emission point

- onset date and termination date of emission in the YYYYMMDDHH format. In v2023r1, the emission duration must be an entire number of hours, and at least one hour.

- Emitted tracer mass

- Minimum and maximum altitude of emission. The tracer mass will be distributed evenly between between these two altitudes

- f_1, f_2, f_3: fraction of tracer mass in the first (resp. 2nd, 3rd) size mode. The user must check that $f_1 + f_2 + f_3 = 1$.

- D_1, D_2, D_3: mass median diameter of the first (resp. 2nd, 3rd) size mode

- σ_1, σ_2, σ_3: multiplicative spread of the first (resp. 2nd, 3rd) size mode ($\sigma_i > 1$)

The proportion of tracer mass between diameters D_m and $D_M > D_m$ is:

$$
\frac{m(D_m \to D_M)}{m} = \sum_{i=1}^{3} f_i \left[\mathrm{erf} \left(\frac{\ln D_M - \ln D_i}{\sqrt{2} \ln \sigma} \right) \right.
$$
10
$$
\left. - \mathrm{erf} \left(\frac{\ln D_m - \ln D_i}{\sqrt{2} \ln \sigma} \right) \right] \tag{1}
$$

4 New landuse

The pre-processing for the CHIMERE specific nine classes landuse was removed in this version. We made the choice to directly use the landuse generated by the WRF Pre-Processing System (WPS) its output geog file. This permits (i) to be faster to prepare in pre-processing, (ii) to be consistent with the meteorology when the two models WRF and CHIMERE are coupled, (iii) to be
15 consistent with the subgrid scale approach of the mineral dust emissions. Changing the landuse classes imposed an update of the surface information required for turbulence, resuspension, albedo calculations and dry deposition. The surface information required for a simulation are presented in Table 1.

The use of a new tabulated dynamical roughness is done by using the values proposed by the WRF model, already fitted for the USGS landuse. The seasonality is considered by using the WRF Green Vegetation Fraction (GVF) as a proxy, with the
20 equation:

$$
z_{0m} = (1 - GVF) \times z_{0m,min} + GVF \times z_{0m,max} \tag{2}
$$

In Table A1, the last z_{0m} value, representative of water surface, is here set to zero but later calculated using the Charnock scheme, (Charnock, 1955). Following the same way, the albedo values are tabulated and are presented in Table A2. It impacts the calculation of the resuspension: with the new landuse, the resuspension is applied for all cell percentages related to urban
25 and agricultural areas following USGS landuse classification. It also impacts the dry deposition and a new correspondence matrix was defined between the EMEP, (Emberson et al., 2001) and the USGS landuse classes.

Name	Description	dimension
dms_<dom>.nc	(Lana et al., 2011)	
DMS	DMS emissions	(x, y, nmonth)
EFMAP_LAI_<dom>_MOD.nc	(Sindelarova et al., 2014; Yuan et al., 2011)	
isoprene, a-pinene etc.	Emission factor of biogenic species	(x,y)
LAI1...LAI46	Leaf Area Index for MEGAN. One map each 8 days	(x,y)
geog_<dom>.nc		
LANDMASK, LANDUSEF, LU_INDEX, HGT_M, SOILTEMP, ALBEDO12M, GREENFRAC, VAR_SSO	landuse, soil, orography, albedo prepared by WRF/WPS	(x, y, nmonth)
LUusgs_z0_erod_<dom>.nc	(Prigent et al., 2012; Beegum et al., 2016; Journet et al., 2014)	
z0aeolian	aeolian z0	(x,y,nland,nsoil)
erodibility	MODIS erodibility	(x,y,nland,nsoil,nmonth)
landuse_index	USGS landuse	(x,y,nland,nsoil)
ratiol	% of soil in each landuse	(x,y,nland,nsoil)
lu_pct	% of landuse in each cell	(x,y,nland)
soil_pct	% of soil in each cell	(x,y,nsoil)
mineral_code	List of mineral codes	(nsoil)
mineral_frac	List of mineral fractions	(nsoil,nmineral)

Table 1. *Files and variables required to proceed a CHIMERE simulation.*

5 New calculation for the turbulence

All calculations dedicated to turbulence were grouped into a single Fortran module. Some parameterizations were updated at the same time. Compared to the CHIMERE version v2020r1, this new module includes the following changes:

5 • The roughness length over the sea, z_0, is not tabulated but calculated using the Charnock's equation, (Charnock, 1955).

• The parameterization of Q_0 and the aerodynamic resistance r_a were upgraded to a more recent scheme. For r_a, its calculation is now on the CHIMERE vertical levels and not on meteorological vertical grid.

• The calculation of turbulent parameters are now in a loop to ensure consistency between all variables (it includes Monin-Obukhov length calculation).

10 • It is now possible to diagnose the 10m wind speed $|U|_{10m}$, the one of WRF being dependent on the boundary layer height scheme and not always satisfying.

5.1 Variables to read or diagnose

In the CHIMERE model, many boundary layer related variables can be diagnosed. But if the meteorological driver model provides some of them, they could be read directly and then used to diagnose the missing ones. The variables that can be read are selected in the *chimere.par* file as:

- *idiagblh*: Use boundary layer height of the meteo driver (idiagblh=0) or diagnose it (idiagblh=1) following Troen and Mahrt (1986).

5 - *idiagflux*: Use the surface turbulent characteristics as the friction velocity u_* and the surface sensible heat flux Q_0 of the meteo driver (idiagflux=0) or diagnose it (idiagflux=1) following Troen and Mahrt (1986).

Depending on this choice, the list of variables that can be read or diagnosed and those that can be diagnosed only is presented in Table 2.

Name	Variable	Unit	Type
U_{10m}	10m wind speed component	$(m.s^{-1})$	R or D
u_*	friction velocity	$(m.s^{-1})$	R or D
$\overline{h}$	boundary layer height	(m)	R or D
H_0	surface sensible heat flux	$(K.m^{-2}.s^{-1})$	R or D
LE_0	surface latent heat flux	$(K.m^{-2}.s^{-1})$	R or D
w_*	vertical convective velocity	$m.s^{-1}$	D
R_{iB}	bulk Richardson number	a.d.	D
L	Monin-Obukhov length	(m)	D
K_z	Vertical turbulent diffusivity	$(m^2.s^{-1})$	D

Table 2. *List of variables required to describe the turbulence in and above the boundary layer. R for "read" and "D" for diagnostic.*

For all calculations, several constants are defined in the code. They can be modified by the user, but it is not really recom-
10 mended. These constant values are listed in Table 3.

5.2 Diagnostic of meteorological variables

Before starting the calculation of the turbulent parameters, it is necessary to estimate some other variables. A specific order is required, some variables being estimated using other variables.

First, the **surface pressure** P_{surf} is simply diagnosed using the pressure values at the two first model levels:

$$P_{surf} = P_1 + \frac{z_1(P_1 - P_2)}{z_2 - z_1} \tag{3}$$

The same calculation is applied to estimate the surface values of specific humidity, cloud liquid content, ice content and rain. The surface values of wind components are set to zero. The total amount of water in the atmosphere is:

$$wa(z) = cliq(z) + cice(z) + rain(z) \tag{4}$$

Parameter	Value	Description	Unit
z10m	10.	10 meters above ground level	m
soimdef	1.0	Default Soil Moisture	m^3/m^3
Vertical turbulent diffusivity boundaries			
vkminup	0.1	Minimum Kz above PBL	m^2/s
vkmax	500.	Maximum Kz	m^2/s
vkmindry	0.01	Minimum Kz in the dry boundary layer	m^2/s
vkminwet	1.0	Minimum Kz in cloudy boundary layer	m^2/s
Boundary layer			
ric	0.5	Troen and Mahrt suggestion for critical Ri for BL top	ad.
ztherm	25.0	Height of thermals start	m
pblmin	20.	Minimum PBL height	m
dvsca	1000.0	Entrain./Detrain. first guess vertical scale	m
Urban suggrid effects			
addwind	0.8	Urban wind correction factor	m/s
addflux	0.	Urban Q_0 correction additive term	m^2/s^2
woff	0.5	Wind offset to smooth Richardson numbers	m/s
Relative humidity and cloud attenuation			
crhx	0.90	Min RH for cloud BLH enhancement	[0:1]
crhh	0.95	High cloud option for attenuation	ad.
cloh2	0.005	High clouds optical depth /m for RH=1	ad.
rlam	150.	Upper air mixing length	m
rhmax	1.2	Maximum acceptable RH	[0:1]

Table 3. *Constant values used for the calculation of additional parameters in the routine calc_turb.*

with $cliq$, $cice$ and $rain$ are the cloud, ice and rain water mixing ratio (kg/kg). The **potential temperature** θ is calculated as:

$$\theta(z) = T(z) . \left(\frac{P_0}{P(z)}\right)^{R_a/C_p} \tag{5}$$

with T the air temperature (K), P_0=10000 Pa the reference pressure, R_a=287.04 J K^{-1} kg^{-1} the specific gas constant for dry air, C_p=1005 J K^{-1} kg^{-1} the specific heat capacity of air. Note that the ratio R_a/C_p is also noted and used as γ=0.2857. The **virtual potential temperature** θ_v is the equivalent of θ but accounting for dry and humid air, as:

$$\theta_v(z) = (1 + 0.61q(z)) T(z) \left(\frac{P_0}{P(z)}\right)^{R/C_p} \tag{6}$$

The **wind speed module**, $|U|$, (m.s^{-1}) is expressed as:

$$|U|(z) = \sqrt{u^2 + v^2} \tag{7}$$

Air density is calculated in (kg.m^{-3}) as:

$$\rho = \frac{P}{R_a \cdot T}.$$
(8)

5   Air density is then converted in (molecules.m^{-3}) with:

$$\rho_{molec/cm3} = \rho_{kg/m3} \frac{N_A}{10^{-3} M_{air}}$$
(9)

with N_A=6.022 10^{23} mol^{-1} and M_{air}=29 g.mol^{-1} the molar mass of air. Note that the multiplication is replaced in the calculation by its result 7.2868 10^{22}.

For the calculation of **relative humidity**, RH, the partial pressure of water vapor e_* (Pa) is first estimated following Tetens's

10   formula (1930) as:

$$e_* = 611.exp\left[17.27\left(\frac{T - T_0}{T - 35.86}\right)\right]$$
(10)

with T_0=273.15K. The dew point, in g/g, is deduced as:

$$de = 0.622 \frac{e_*}{P - e_*}$$
(11)

Finally, the relative humidity is calculated as:

15    $$RH = \frac{q}{de}$$
(12)

The relative humidity is protected against extreme values and bounded to the 'rhmax' constant value defined in Table 3.

One key point for turbulence parameterizations is to diagnose the near-surface virtual potential temperature, here noted $\theta_{v,0}$. To access this value, we extrapolate the vertical temperature profile by using the 2m temperature T_{2m} and the temperature at the first model vertical level, T_1 to obtain T_0. The following expression is used:

20    $$T_0 = T_{2m} - \frac{z_{2m}\,(T_1 - T_{2m})}{z_1 - z_{2m}}$$
(13)

Over sea, it is common to use the Charnock's equation to estimate the momentum roughness length, dependent on the sea surface and the waves height:

$$z_0 = \alpha_c \frac{u_*^2}{g}$$
(14)

where α_c is a constant as $\alpha_c \approx 0.015$. Pena and Gryning (2008) note that this constant could ranged between 0.008 and 0.06 depending on the studies. The roughness length depending on the friction velocity, and vice versa, an iterative approach is necessary to quantify the two. Fortunately, Hersbach (2011) proposes an efficient fit to estimate z_0 without knowledge of u_*.

$$z_0 = \frac{z}{exp(b_n) - 1}$$
(15)

with $b_n = [(b_n^\nu)^p + (b_n^\alpha)^p]^{1/p}$, and p=-12. The two parameters expressed that z_0 depends on kinmatic viscosity ν for light wind and on Charnock relation for strong wind. They are estimated with:

$$
\begin{aligned}
b_n^\nu &= -1.47 + 0.93 ln(R) \\
R &= \frac{z}{\alpha_M \nu}(k u_n) \\
b_n^\alpha &= +2.65 - 1.44 ln(A) - 0.015(log(A))^2 \\
A &= \frac{\alpha_{ch}}{g\, z}(k u_n)^2
\end{aligned}
\tag{16}
$$

with k=0.41, the Von Karman constant, ν=1.5 10^{-5} m^2 s^{-1}, the kinematic visocosity, u_n the wind speed at height z (here z=10m), α_M=0.11 and α_{ch}=0.018, the Charnock constant. This roughness length calculated for three different Charnock constants is displayed in Figure 3.
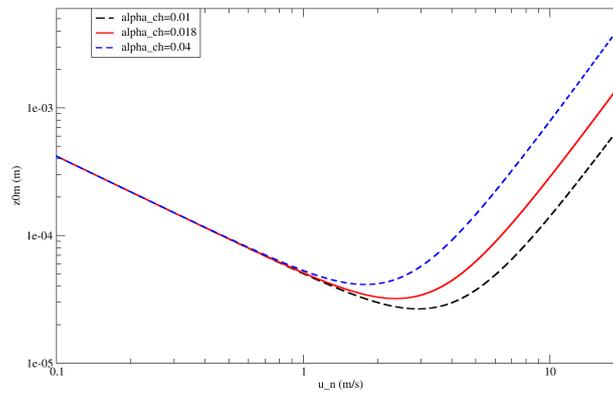
Figure 3. *Roughness length over water surfaces calculated for three different Charnock constants*

5.3 Optical depth above model top

In order to have the optical thickness due to clouds for the full tropospheric column, an optical depth is estimated above the CHIMERE domain top and using the meteorological model data. It is generally possible since the CHIMERE model has currently a model top around 200 hPa (user's choice) when the meteorological model has a model top around 50 hPa. For the atmospheric column in CHIMERE, the Fast-JX module calculates directly the Cloud Optical Depth (COD). The top level of CHIMERE, $ptop_{chimere}$, is first estimated in the meteorological model grid. The following equation is then used:

$$
COD_{above} = \sum_{ptop_{chimere}}^{ptop_{meteo}} \frac{5.10^{-3}.(\overline{RH} - 0.95).\Delta z}{1 - 0.95}
\tag{17}
$$

where 0.95 is the value of high cloud attenuation and 5.10^{-3} is the high clouds optical depth for RH=1 and in m^{-1}. $ptop_{meteo}$ is the pressure of the top level of the meteorological model. Finally, the attenuation due to cloud above the model top is estimated using the empirical formula:

10 $$A_{top} = exp(-0.11.COD_{above}^{2/3}) \tag{18}$$

5.4 Urban correction

A simple urban correction is available in the model. This is very simple and just implemented to retrieve some observed trends: less surface wind speed and more surface sensible heat flux. This option may be activated in the *chimere.par* parameter file by changing the *urbancorr* flag. This activation induces a slight change for the wind speed in the surface layer (from ground to

15 surface layer height) and Q_0 the surface sensible heat flux, only over urbanized areas as:

$$U_{10m,urb} = factU \times U_{10m} \tag{19}$$
$$Q_{0,urb} = addflux + Q_0 \tag{20}$$

The factor for the wind speed is equal to the proportion of urban surface in the cell multiplied by a factor defined in the module *calc_turb.F90* as a parameter, *factU*. A usual default value is 0.8. The change for Q_0 is an additionnal flux called

20 *addQ0* and equal to 30 $W.m^{-2}$. These values may be changed directly in the model code. Note that this correction is applied to the wind profile (u,v) before the diagnostic of turbulent fluxes and after the diagnostic of Q_0.

5.5 Diagnostic of turbulent variables

It is possible to directly use the turbulent variables calculated by the meteorological forcing model. For that, two conditions have to be fullfiled: (i) the flag *idiagflux*=1 in *chimere.par* and (ii) the corresponding variables, friction velocity u_* and surface

25 sensible heat flux Q_0, must be available in the meteorological model outputs. If these two conditions are not reached together, these variables have to be diagnosed, each variable being dependent on the others. Due to these dependencies, it is an iterative process.

5.5.1 The Richardson number

First, a calculation of the surface layer turbulent variables must be done. It is necessary to calculate the stability of the atmo-

5 sphere. Following the scheme of Jiménez et al. (2012), the bulk Richardson number is calculated:

$$Ri_b = \frac{g\,z}{\theta_a}\,\frac{\theta_{va} - \theta_{vg}}{U^2} \tag{21}$$

with θ_{vg} and θ_{va} (K) the virtual potential temperature at ground and first model levels, respectively. The first vertical model level is at height z. g is the acceleration of gravity. U is the mean wind speed at altitude z. To avoid too large and unrealistic values of Ri_b, a minimum value of $U = 0.1$ m.s^{-1} is forced.

10 The Monin-Obukhov length L is iteratively estimated using the first guess value of Ri_b using the equation:

$$Ri_b = \frac{z}{L} \frac{\Psi_T}{\left[ln\left(\frac{z+z_{0m}}{z_0}\right) - \psi_m\left(\frac{z+z_{0m}}{L}\right) + \psi_m\left(\frac{z_{0m}}{L}\right)\right]^2} \tag{22}$$

with Ψ_T equal to:

$$\Psi_T = ln\left(\frac{z+z_{0h}}{z_{0h}}\right) - \psi_h\left(\frac{z+z_{0h}}{L}\right) + \psi_h\left(\frac{z_{0h}}{L}\right) \tag{23}$$

z_{0m} is the momentum roughness length and is tabulated. For the heat roughness length, having no specific information about
15 it, the simple relation of Beljaars and Holtslag (1991) is used as: $z_{0h} = z_{0m}/10$. Note that in Jiménez et al. (2012), all equations are using only "z_0" without distinction between momentum and heat. We thus apply here the relation $z_{0h} = z_{0m}$, because the use of a lower z_{0h} gives too low surface sensible heat flux. The stability functions $\psi_m(z/L)$ (for momentum) and $\psi_h(z/L)$ (for heat) are calculated using the modified formulation of Jiménez et al. (2012) such as:

1. If $Ri_b > 0.$ (nocturnal stable boundary layer):

$$\begin{cases} \psi_m = -a \; ln\left[\frac{z}{L} + \left[1 + \left(\frac{z}{L}\right)^b\right]^{1/b}\right] \\ \psi_h = -c \; ln\left[\frac{z}{L} + \left[1 + \left(\frac{z}{L}\right)^d\right]^{1/d}\right] \end{cases} \tag{24}$$

with a=6.1, b=2.5, c=5.3 and d=1.1.

2. If $Ri_b \leq 0$ (free unstable conditions):

$$\psi_{h,m} = \frac{\psi_{K,h,m}\left(\frac{z}{L}\right) + \left(\frac{z}{L}\right)^2 \psi_{C,h,m}\left(\frac{z}{L}\right)}{1 + \left(\frac{z}{L}\right)^2} \tag{25}$$

5 where $\psi_{C,h,m}$ represents the convective contribution as:

$$\psi_{C,h,m} = \frac{3}{2} ln\left(\frac{y^2+y+1}{3}\right) - \sqrt{3} \, arctan\left(\frac{2y+1}{\sqrt{3}}\right) + \frac{\pi}{3} \tag{26}$$

with $y = [1 - \alpha_{h,m} (z/L)]^{1/3}$. $\alpha_m = 10$ and $\alpha_h = 34$, after Grachev et al. (2000). $\psi_{K,h,m}$ represents the "Kansas type" contribution as initially proposed by Paulson (1970) such as:

$$\begin{cases} \psi_m = 2\,ln\left(\dfrac{1+x}{2}\right) + ln\left(\dfrac{1+x^2}{2}\right) - 2arctan(x) + \dfrac{\pi}{2} \\ \psi_h = 2\,ln\left[\dfrac{1+\sqrt{1-\gamma\left(\dfrac{z}{L}\right)}}{2}\right] \end{cases} \tag{27}$$

with $x = [1 - \gamma(z/L)]^{1/4}$ and γ=16.

5.5.2 The friction velocity u_*

The friction velocity u_* and the potential temperature scale θ_* are calculated as Beljaars and Holtslag (1991):

$$u_* = \frac{kU}{ln\left(\dfrac{z+z_{0m}}{z_{0m}}\right) - \psi_m\left(\dfrac{z+z_{0m}}{L}\right) + \psi_m\left(\dfrac{z_{0m}}{L}\right)} \tag{28}$$

$$\theta_* = \frac{k\,(\theta_a - \theta_g)}{ln\left(\dfrac{z+z_{0h}}{z_{0h}}\right) - \psi_h\left(\dfrac{z+z_{0h}}{L}\right) + \psi_h\left(\dfrac{z_{0h}}{L}\right)} \tag{29}$$

Note we also added here the correction term with $(z+z_{0m,h})$ in place of (z). For the first iteration, we can calculate u_* and θ_* under neutral conditions, considering ψ_m and ψ_h equal to unity. The Monin-Obukhov length L is then updated as:

$$L = \frac{\theta_a u_*^2}{k\,g\,\theta_*} \tag{30}$$

The iterative algorithm may be summarized as:

1. Ri_b is calculated using the meteorological variables in equation 21

2. L is estimated using the equation 22 and considering neutral conditions to have $\psi_m = \psi_h = 0$.

3. A loop is then performed with:

   (a) Calculation of ψ_m and ψ_h with the updated (z/L) value

   (b) Calculation of u_* and θ_* using the updated ψ_m and ψ_h

   (c) Calculation of L using the updated u_* and θ_*

and the iterations stop when two successive values of L are lower than a pre-defined threshold. Here, we use ΔL=0.1. After several tests, the convergence is generally reached after four iterations.

The 10m wind speed is then diagnosed as:

$$u_{10m} = u_a \frac{ln\left(\frac{10+z_{0m}}{z_{0m}}\right) - \psi_m\left(\frac{10+z_{0m}}{L}\right) + \psi_m\left(\frac{z_{0m}}{L}\right)}{log\left(\frac{z+z_{0m}}{z_{0m}}\right) - \psi_m\left(\frac{z+z_{0m}}{L}\right) + \psi_m\left(\frac{z_{0m}}{L}\right)} \tag{31}$$

5.5.3 The surface heat fluxes

The surface heat fluxes are not always provided in forcing models. But we need this quantity to evaluate w_* and $\overline{h}$. For its quantification, there is two ways. First, we have the information about the sensible H (W.m^{-2}) and latent LE (W.m^{-2}) turbulent fluxes (the "eddy fluxes"). We can thus estimate the fluxes close to the surface as:

$$\begin{cases} \overline{w'T'}_0 = \overline{(H+H_{urb})}.\frac{R}{C_p}.\frac{T_{2m}}{P_{surf}} \\ \overline{w'q'}_0 = \overline{LE}.\frac{R}{L_v}.\frac{T_{2m}}{P_{surf}} \end{cases} \tag{32}$$

with R=287.04 J kg^{-1} K^{-1}, C_p the specific heat capacity (C_p=1005 J.K^{-1}.kg^{-1}), L_v the latent heat of vaporization (L_v=2.45 10^6 J.kg^{-1}). H_{urb} is an additional surface sensible heat flux, representing an urban contribution, and chosen as H_{urb}=0 by default. A value of H_{urb}=30 W.m^{-2} is often used in regional or urban modeling. The total (heat + latent) surface flux, Q_0, is then estimated as:

$$Q_0 = \overline{w'T'}_0 \times (1+0.61q) + \overline{w'q'}_0 \times 0.61 \times \theta_0 \tag{33}$$

Second, if we have no information, we use the previous parameterized values of u_* and θ_*. Q_0 is estimated as:

$$Q_0 = -u_*\theta_* \tag{34}$$

5.5.4 The boundary layer height $\overline{h}$

If the boundary layer height ($\overline{h}$) is available in the meteorological model and if it is the user's choice, the variable is just read, not calculated. If the user prefers to have a diagnostic made in CHIMERE, the calculation is done as follows. To select the use of the meteorological model, the two following conditions must be reached: (i) the boundary layer height $\overline{h}$ must be available in the meteorological model outputs, the flag *idiagblh* must be 0 in *chimere.par*.

In case of diagnostic, the following calculation is performed. Formulations are different depending on the atmospheric static stability. When stable, i.e when $L > 0$, $\overline{h}$ is estimated as the altitude when the Richardson number reaches a critical number

here chosen as R_{ic}=0.5, following Troen and Mahrt (1986). Under unstable situations (i.e. convective), $\overline{h}$ is estimated using a convectively-based boundary layer height calculation. This is based on a simplified and diagnostic version of the approach of Cheinet and Teixeira (2003) which consists in the resolution of the (dry) thermal plume equation with diffusion. The in-plume

10 vertical velocity and buoyancy equations are solved and the boundary layer top is taken as the height where calculated vertical velocity vanishes. Thermals are initiated with a non-zero vertical velocity and potential temperature departure, depending on the turbulence similarity parameters in the surface layer. The two formulations are used and the maximum of the two diagnosed $\overline{h}$ is retained.

5.5.5 The free convection velocity scale w_* and the aerodynamical resistance r_a

15 Now that we have the boundary layer height $\overline{h}$, it is possible to more properly estimate the free convection velocity scale w_*:

$$w_* = \left(\frac{g.Q_0.\overline{h}}{\theta_{v,a}} \right)^{1/3} \tag{35}$$

where $\overline{h}$ is the convective boundary layer height, C_p the specific heat of air at constant pressure, $\overline{\theta_{v,a}}$ the mean virtual potential temperature at the first model vertical level. For the aerodynamical resistance, we use the Bruin and Holtslag (1982) equations such as:

20 $$r_a = \frac{4.72 \left[ln \left(\frac{z}{z_{0m}} \right) \right]^2}{1 + 0.54 U} \tag{36}$$

with U the wind speed at height z (in our case the first vertical model level). Note that Bruin and Holtslag (1982) are using a fit with the momentum roughness length z_{0m}, when the usual expression of r_a is using the heat roughness length. This fit replaces the regular expression of the aerodynamical resistance, Beljaars and Viterbo (1994), as:

$$\frac{1}{r_a} = \frac{k \, u_*}{ln \left(\frac{z + z_{0h}}{z_{0h}} \right) - \Psi_h \left(\frac{z + z_{0h}}{L} \right)} \tag{37}$$

5.5.6 Momentum vertical turbulent diffusivity K_z

The momentum turbulent diffusivity K_z (m^2.s^{-1}) has different formulations, depending on the period of the day (stable or unstable conditions) and the altitude (surface layer, mixed layer, free troposphere).

5 In the **surface layer**, when conditions are stable, the turbulence is the most difficult to diagnose, the variances of meteorological variables being very small. Troen and Mahrt (1986) remind that the surface layer is considered in equilibrium, then the

parameterization of Louis (1979) is used. In the **mixed layer**, K_z is calculated following the parameterisation of Troen and Mahrt (1986), without counter-gradient term as:

$$K_z = k \, w_s \, \overline{h} \, \frac{z}{\overline{h}} \left(1 - \frac{z}{\overline{h}} \right)^2 \tag{38}$$

where k=0.41 the Karman constant, z the altitude, $\overline{h}$ the boundary layer height and w_s a vertical velocity scale. Note that the formulation in Troen and Mahrt (1986), equation 1 is false. The calculation of w_s depends on the atmospheric stability. For the stable case:

$$w_s = \frac{u_*}{(1 + 4.7 \, z/L)} \tag{39}$$

and for the unstable case:

$$w_s = (u_*^3 + 7 \, \epsilon \, k \, w_*^3)^{1/3} \tag{40}$$

where L is the Monin-Obukhov length (m), g=9.81 m^2.s^{-2} the gravitational acceleration and θ_v the virtual potential temperature in Kelvin. $\overline{\theta_v}$ corresponds to the mean average in the first vertical model layer. The constant ϵ is defined as 0.1 in Troen and Mahrt (1986). For the model, this value is defined as $e = min(0.1, z/\overline{h})$ to ensure a robust calculation in the first vertical model levels. To avoid numerical problems, values of K_z are bounded using predefined constants values, as explained in Table 4.

Name	Value	Function
$K_{z,min,dry}$	0.01	Minimum K_z in the dry boundary layer
$K_{z,min,wet}$	1.	Minimum K_z in the cloudy boundary layer
$K_{z,min,up}$	0.1	Minimum K_z above the boundary layer
$K_{z,max}$	500.	Maximum K_z

Table 4. *Boundaries for the K_z diagnosed values (in $m^2.s^{-1}$).*

Above the boundary layer, and in presence of clouds, an additionnal diffusivity is added. This diffusivity is estimated if the relative humidity if larger than 0.9. For each model vertical level, a new vertical diffusivity K_z is estimated. The formulation is inspired by the Betts et al. (1995) study and the implementation of the turbulence scheme in the NCEP operational Medium-Range Forecast (MRF) Model. The concept is based on the Louis (1979) formulation, defining stability function.

The vertical diffusion coefficient $K_{z,m,h}$ (as a function of altitude z, and for momentum m and heat h) is here expressed as:

$$K_{z,m,h} = l_{mix}^2 \, f_{m,h}(R_{ib}) \left| \frac{\partial U}{\partial z} \right| \tag{41}$$

where: Ri is the local gradient Richardson number, U the wind speed module, z the altitude, $f_{m,h}$ the stability function for momentum and heat, and l the mixing length diagnosed as:

$$\frac{1}{l} = \frac{1}{k\,z} + \frac{1}{\lambda_c} \tag{42}$$

with k the von Karman constant, λ_c, the asymptotic length scale with λ_c=150m (but 250m in (Betts et al., 1995)). The stability function f_m and f_h are estimated as:

$$f_m = \begin{cases} 1 + 8\left(\dfrac{-Ri}{1 + C_{m,h}\,\sqrt{Ri}}\right) & \text{For Ri} < 0 \text{ (unstable)} \\[4mm] \dfrac{1}{(1 + 5\,Ri)^2} & \text{For Ri} \geq 0 \text{ (stable)} \end{cases} \tag{43}$$

with C_m=1.746 and C_h=1.286.

6 Changes in emissions

Emissions are the main chemical forcings of the model. In parallel with the development of the CHIMERE model itself, the various emissions taken into account are also updated between two versions. This section therefore presents newly taken into account emissions as well as updated and improved ones.

6.1 Changes in anthropogenic emissions

The management of the anthropogenic emissions has changed in this version of the model. The goal is to have fewer files to manage, a sore point on supercomputers. The new format corresponds to one file per type of day of the week, so seven files per month. Indeed, we have temporal data to differentiate the months of the year, the days of the week in a month and the 24 hours of a day.

All chemical emitted species are grouped together in each files (before it was one file per species). For each species, the resolution is hourly and the fluxes are projected on the horizontal grid of the model. By using the provided EMISURF program, the user can also choose to differentiate his emissions fluxes by activity sector according to the GNFR nomenclature. This differentiation will then be necessary in case of simulation using the sub-grid variability option.

Finally, the user is encouraged to use the emisurf model (described in Mailler et al. (2017)) developed by the CHIMERE model team. This model is able to ingest multiple input databases, as described in Table 5. In its latest version (v2023r1), emisurf takes into account the most recent time factors data (Guevara et al., 2021; Crippa et al., 2020).

	EMEP	HTAP	CAMS	RCP8.5
Grid Resolution	$0.1^o \times 0.1^o$	$0.1^o \times 0.1^o$	$0.1^o \times 0.1^o$	$0.5^o \times 0.5^o$
Totals	Annual	Annual/Monthly	Monthly	Monthly
Available years	1990-	2000-2018	>=2000	2000,2005,2010
				2020, 2030, 2040
				2050, 2060, 2070
				2080, 2090, 2100
Reported pollutants	CO, NH_3, NMVOC NO_X,SO_X, $PM_{2.5}$ PM_{10},PM_{Coarse}	CO, NH_3, NMVOC NO_X,SO_2, $PM_{2.5}$ PM_{10},BC, OC	CO, NH_3, NMVOC NO_X,SO_2,CO_2 BC, OC	CO, NH_3, NMVOC NO_X,SO_2,CH_4 BC, OC
Spatial coverage	Europe	Global	Global (CAMS_GLOB_ANT) and Europe (CAMS_REG)	Global
Activity sectors	GNFR14	Industry, Energy Residential, Transport, Air, Ship Agriculture	Industry, Energy Residential, Road transport Fugitives, Solvents, Off road Transport, Ships, Waste Agriculture (+livestock)	Industry, Energy Residential, Solvents Land Transport, Waste Agriculture Agricultural Waste
Download	https://www.ceip.at/	https://edgar.jrc.ec.europa.eu	https://eccad3.sedoo.fr/	http://www.iiasa.ac.at

Table 5. *The different anthropogenic emission inventories processed by the emiSURF model.*

6.2 Implementation of pollen emission

Pollen emissions were taken into account in a parallel version of CHIMEE operated by INERIS for the Copernicus daily
10   forecast over Europe. The code was cleaned and is now implemented in the official CHIMERE version. It means that from
now, pollen emission, transport and deposition will be always available in CHIMERE.

6.2.1 The pollen grains specificities

Pollen grains are very different from the usual atmospheric aerosols. About their transport, Sofiev et al. (2006) showed that
they can be transported together with air masses and may be mixed due to small turbulent eddies. In this model version, five
different pollen species were implemented: birch, olive, ragweed, grass and alder. The pollen density depends on each species
and varies between 800 and 1200 kg.m^{-3}, which yields the sedimentation velocity of 1.2-1.3 cm.s^{-1}. The main dry deposition
5   process for pollens is gravitational settling and they can be washed out by rains. For pollen, only the 'big' mode of the aerosol
is designed. The pollen species are considered as non-chemically reactive. Optical properties are prescribed for short-wave and
long-wave wavelengths.

6.2.2 Main principle of emissions for birch, grass and olive

To calculate pollen emissions, several surface databases are needed. In this model version, the databases are limited to western
Europe. Three parameters are needed for each species: the surface fraction, the heat sum threshold and a scale factor. For the
grass pollen, the data come from the SILAM model (Sofiev et al., 2006). Some additional information are provided: the mean
diameter, D_p=32 μm, the density 800 kg.m^{-3} and the height above surface, h=1 m. Note also there is no time dependency in
this database. It is probably to improve later, since the ragweed locations increase every year in Europe (Schaffner et al., 2020).

The pollen emissions modeling is challenging because it requires a fair knowledge of plant distribution, phenology, and
adequate assumptions regarding the sensitivity to meteorological factors, such as humidity, temperature, wind speed and turbu-
lence. Unlike industrial pollutants or mineral aerosols, pollen emissions depend not only on the instantaneous meteorological
conditions but also on the conditions during the pollen maturation within the plants before the pollination starts: it means that
an accurate simulation required to start several months before the targeted period. For all species, emissions schemes have the
same basis, as:

$$E(x,y,t) = D(x,y) \times P(x,y,t) \times \phi(x,y,t) \times R(x,y,t) \qquad (44)$$

where $D(x,y)$ is the ragweed density distribution in number of individual plants per square meter. $P(x,y,t)$ is the annual
production in grains per individual plant. $\phi(x,y,t)$ is the phenology factor in s^{-1}, considering its yearly integrated value is
unity. This factor represents the knowledge of the start and end date of the pollen season as well as the shape of these potential
emissions. $R(x,y,t)$ is the daily or sub-daily weather-dependent release of pollen grains in the atmosphere which depends
on the hourly (or daily) meteorological variables. $R(x,y,t)$ is unitless. These different terms correspond to two different
temporal scales: $D(x,y)$, $P(x,y,t)$ and $\phi(x,y,t)$ represent "annual" information, when $R(x,y,t)$ represents the "short-term"
information for which we want to evaluate correlation with the meteorological variables.

To calculate these terms, we used the scheme of Prank et al. (2013) (referred to as P2013 hereafter). It is the scheme used
in the SILAM model, Sofiev et al. (2013). Originally developed for birch pollen, it was adapted to ragweed by Prank et al.
(2013). It is also used for Olive, Grass and Alder. This SILAM version is directly implemented in CHIMERE and used without
any changes. This scheme is based on a double-heat sum concept (Linkosalo et al., 2010). The temperature accumulates
from the 60th day of the year (February 29 or March 1), and when the accumulated heat sum reaches the first threshold the
flowering season starts. The end of the flowering season occurs when there is no more pollen left in the catkins (the open-pocket
principle). The model not only predicts the start and the end of the flowering season, but also relates the amount of pollen ready
to be realeased to the stage of the bud development. The actual pollen release during the flowering season is determined by
meteorological factors, (Sofiev et al., 2013). The model also takes into account the fact that different trees within the same
model grid cell get ready to emit pollen at slightly different times, with a few days difference. As a result the model calculates
the pollen emission flux as a function of time. The emission flux is determined by the spatial distribution of birch trees, by the
heat sum threshold distributions, and by meteorological conditions during the flowering season.

In terms of seasonal emission flux modulation, three time periods are distinguished:

- Before the beginning of the flowering season, the emission rate is zero and the heat sum H is accumulated starting from a certain date D_s until it reaches some flowering-start threshold H_{start}

- During the flowering season, as H continues to accumulate, pollen emission rate R(t) grows;
- The pollen season is over, as soon as there is no more pollen in the catkins (the open-pocket principle).

Summing up, the pollen emission is determined by the following factors:

1. The heat sum exceeding a certain threshold value H_{start} in a gridpoint ($H(t) > H_{start}$)

2. The temperature exceeds the cut-off value T_{co} ($T > T_{co}$)

3. The meteorological parameters that inhibit emissions, unless having their optimal values (humidity, rain) or stimulate emissions via mechanical action (wind speed, convective turbulence);

4. Available pollen in catkins ($N_{tot} \neq 0$);

5. Trees are flowering (F_{in} and $F_{out} \neq 0$).

20   The resulting emission flux E is a product of the above-described terms:

$$
\begin{aligned}
E(t,i,j) \quad = \quad & N_{tot} \times \phi(i,j) \times \frac{T - T_{co}}{\Delta H} \times f_{wind}(U, w^*) \\
& \times F_{in}(\frac{H}{H_{start}}) \times F_{out}(\frac{R(t)}{N_{tot}}) \\
& \times f_{th}(q, q_{low}, q_{high}) \times f_{th}(P, P_{low}, P_{high})
\end{aligned}
\tag{45}
$$

where :

- N_{tot} (grains.m^{-2}.year^{-1}) is the total number of pollen grains released from 1 m^2 during the whole year.
- ϕ(i,j) is the pollen plant fraction in grid cell (i,j).
- $\frac{T-T_{co}}{\Delta H}$ is a relative emission intensity as a linear function of temperature.
- F_{in} is the emission flux fraction depending on the relative heat sum.
- F_{out} is the emission flux fraction depending on pollen quantity emitted since the start of the flowering season.
- f_{wind} is the wind speed-dependent correction.
- f_{th} are the coefficients modulating emissions by humidity and precipitation (between 0 and 1).

5   Once the flowering season started, the actual pollen release is determined by meteorological conditions that can either biologically inhibit emissions with respect to an optimal level (humidity and precipitation) or stimulate emission due to mechanical forces (wind and convective turbulence) on the daily basis. The key variables are the wind speed U, the convective velocity scale w^*, the relative humidity q, precipitation rate P, and daily-evolving temperature T.

Precipitation and humidity impacts in the model are governed by the following equation, where x_{low} may be P_{low} or rh_{low}

10 and x_{high} may be P_{high} or rh_{high}. Depending on the pollen species, the values are fixed in Table 6.

$$f_{th} = \begin{cases} 1 & \text{if } x \leqslant x_{low} \\ \dfrac{x_{high} - x}{x_{high} - x_{low}} & \text{if } x_{low} < x \leqslant x_{high} \\ 0 & \text{if } x > x_{high} \end{cases} \tag{46}$$

Parameter	Birch	Olive	Alder	Grass	Ragweed
N_{tot}	10^9	3.10^8	10^8	0.0	10^9
D_s (# days)	60	60	1	60	60
T_{co} (K)	276.65	276.65	277.15	277.15	277.15
Hc (m)	15.	15.	15.	-	1.
P_{low}	0.0	0.0	0.0	0.0	0.0
P_{high}	0.5	0.5	0.5	0.5	0.5
rh_{low}	50.	50.	50.	50.	50.
rh_{high}	80.	80.	80.	80.	80.
δ_{in}	0.2	0.2	0.2	-	-
δ_{out}	0.2	0.2	0.2	-	-
$f_{windmax}$	1.5	1.5	1.5	1.5	1.5
U_{satur}	5.	5.	5.	5.	5.
Delta$_H$	100.	50.	-	-	-

Table 6. *Fixed parameters for the pollen emissions. N_{tot} is the total number of grains per m^2 and year, D_s is the flowering starting Julian day, T_{co} if the temperature cut-off value (K), Hc is the emissions height.*

Wind speed U and convective turbulence w^* impacts are described as:

$$f_{wind} = f_{wind-max} - exp\frac{-(U + w^*)}{U_{satur}} \tag{47}$$

where U_{satur} corresponds to the maximum value where the wind still strengthens emissions, and $f_{wind-max}$ describes the magnitude of wind impact. For birch: U_{satur} = 5 $m.s^{-1}$ and $f_{wind-max}$ = 1.5 (Table 6). All the trees of the same grid cell do

5 not start flowering at the same time, the transition between phenological stages being accomplished in a gradual manner. The gradual start of the flowering of the trees in a grid cell is described by the relative heat sum $x = \frac{H(t)}{H_{start}}$, with the corresponding term $F_{in}(x)$ given by:

$$F_{in}(x) = \begin{cases} 0 & \text{if, } x < 1 - \delta_{in} \\ \frac{x-1+\delta_{in}}{2\delta_{in}} & \text{if, } 1-\delta_{in} \leqslant x < 1+\delta_{in} \\ 1 & \text{if, } x \geqslant 1+\delta_{in} \end{cases}$$

where δ_{in} is a relative uncertainty of H_{start}. The parameter controlling the gradual flowering saison termination is the number of grains remaining in catkins with respect to the initial total number of grains N_{tot}: $x = \frac{R(t)}{N_{tot}}$. In the current model version N_{tot} is fixed, e.g., $N_{tot} = 10^9$ for birch. The corresponding term $F_{out}(x)$ is given by:

$$F_{out}(x) = \begin{cases} 1 & \text{if, } x < 1 - \delta_{out} \\ \frac{x+1-\delta_{out}}{2\delta_{out}} & \text{if, } 1-\delta_{out} \leqslant x < 1+\delta_{out} \\ 0 & \text{if, } x \geqslant 1+\delta_{out} \end{cases}$$

where δ_{out} is a relative uncertainty of N_{tot}.

To simulate the pollen emission flux, the tree spatial distribution maps for each species are required. For birch, It was compiled by Sofiev et al. (2006) from a combination of national forest inventories of Western Europe and satellite images of broadleaf forests when the former information was not available. The forest inventories reveal irregularities, probably related to the specifics of national methodologies for forest surveys. The use of satellite images allows to smooth the data between the countries. Some interpolations were made based on assumptions like: between 62°N and 65°N, the fraction of birch is expected to be equal to that found in Finland (80%). In France, birch are mainly present in the Massif Central (middle mountain region), the West (Bassin Aquitain), and the North-East (les Vosges). As noted by Sofiev et al. (2013), there are noticeable regional variations in the temperature sum threshold necessary to trigger the flowering season. Hence the temperature sum thresholds were fitted into phenological and aerobiological observations independently inside 33 sub-regions of Europe. This yielded a temperature sum threshold map for the flowering season start.

6.2.3 The heat sum concept

The heat sum, HS, concept follows the concept of Chapman et al. (2014), based on Biological Days. Some input information is necessary to update HS at each model time-step: the current 2m temperature, the current day, its length in hours and the time step. The HS is updated only if the current day is after the first day, in our case always equal to 79 (i.e the 20 March). Two ramp functions are estimated, one depending on the 2m temperature, the second one on the day length. All data used are the same as in SILAM as described in Prank et al. (2013), using parameters defined in Deen et al. (1998). The HS is then equal to:

$$HS = HS + r_T \times l_h \times \frac{\Delta T}{86400} \tag{48}$$

with:

$$
r_t = \begin{cases} \dfrac{T - T_{low}}{T_{opt} - T_{low}} & \text{if } T_{low} < T < T_{opt} \\ \dfrac{T_{high} - T}{T_{high} - T_{opt}} & \text{if } T_{opt} < T < T_{high} \end{cases}
\tag{49}
$$

the l_h variable is equal to 1 except if the day length (d_l) is greater than the photo period parameter, here 14.5 and for the
10   following values:

$$
l_h = \begin{cases} exp((d_l - N_{h,ph}) \times log(0.95)) & \text{if } 11.5 < \text{HS} < 16 \\ exp((d_l - N_{h,ph}) \times log(0.94)) & \text{if } 16 < \text{HS} < 20.5 \end{cases}
\tag{50}
$$

where the threshold temperature values are fixed. Note that this HS may be reset to zero depending on specific meteorological
conditions as:

– $T_{2m} < T_{thr}$ (here T_{thr}=273.15K)

15   – daily mean $T_{2m} < dayT_{thr}$ (here $dayT_{thr}$=280.65K). Note that in this model version, the daily mean 2m temperature is
the running average for the last 24h.

– HS is lower than StartHSThr. This value is here fixed to StartHSThr=25.0, following Deen et al. (1998).

With this scheme, there are no emissions during the night. The calculation of sunrise and sunset is necessary. At the end,
note that emissions are injected in the first model level only in CHIMERE, where they are injected in the whole boundary layer
20   in SILAM.

6.2.4   The ragweed emission

The ragweed pollen emission is a specific case. It is possible to use the P2013 scheme but two others are also implemented. The
first one is the scheme developed by Efstathiou et al. (2011) and corresponding to a modified version of Helbig et al. (2004).
The second one is the scheme of Menut et al. (2021b), corresponding to a modified version of Efstathiou et al. (2011).
25   The approach of Efstathiou et al. (2011), hereafter called E2011, is a mix between the schemes of Helbig et al. (2004) and
Sofiev et al. (2006), adapting these formulations to ragweed. In the following, the specific notations of the publications are
used to have a reference. The terminology is different from P2013 and Helbig et al. (2004), but the principle is the same. The
pollen emission flux, E (grain.m^{-2}.s^{-1}), is calculated as:

$$
E = c_e \times c^* \times K_e \times u_*
\tag{51}
$$

The flux depending on the surface grid cell and time, $E(x, y, t)$. The terms of the equation are: c_e a plant specific factor, c^* is the grain production factor. The release factor R_e is represented by $(K_e \times u_*)$. K_e is a time-varying factor depending on weather and u_* is the friction velocity. The plant specific factor, c_e, is calculated as:

$$c_e = 4c_b \left(\frac{d}{S} - \frac{d^2}{S^2} \right) \tag{52}$$

where c_b is approximated to 10^{-4}. S is the pollen season duration in days, with S=60. d is the Julian day, varying during the simulation. In practice, the starting and ending dates of the ragweed period are fixed here to 210 and 270 Julian days, respectively. The grain production factor c^* is calculated as:

$$c^* = \frac{q_p}{LAI \times h_c} \tag{53}$$

where q_p is the total production of grains per year and is 10^9 grains.m^{-2}. It corresponds to the maximum number of emitted grains. Day after day, q_p is reduced by the amount of the already emitted grains the day before. LAI is the Leaf Area Index. LAI is a map in E2011, but in this CHIMERE version, we are using the value of LAI=3. h_c=1 m is the canopy height. The K_e variable is estimated as:

$$K_e = K_h \times K_w \times K_r \tag{54}$$

with the three meteorological limiting factors: K_h for humidity, K_w for 10m wind speed and K_r for precipitation. For relative humidity, the limiting factor is expressed as equation 46 with q_{low}=50% and q_{high} = 80%. For precipitation, we use the fit in E2011 as:

$$K_r = 1. - \frac{p}{0.5} \tag{55}$$

with p the precipitation rate in mm.h^{-1}. For the wind speed, K_w is based on P2013 wind speed correction previously described with equation 47.

The Menut et al. (2021b) scheme, herefater called M2021, has the same formulation as the E2011 scheme, except that the release term is reformulated. The emissions flux is expressed as:

$$E = c_e \times c^* \times R_{TS} \tag{56}$$

where c_e and c^* are the same functions as in the E2011 scheme. R_{TS} is the modified instantaneous release factor. Based on the correlation results in M2021, it appears that the main driving factors are those related to thermodynamical processes,

namely the 2 m temperature, T_{2m}, vertical velocity scale w_* and short-wave radiation SW_d. The pollen emissions may be moderated by precipitation rates P_r and 2 m specific humidity q_{2m}.

The differences between birch and ragweed emissions could be explained by the plant typology itself: birch is a tree, with the pollen source up to 10 m above the ground. At this level, the wind may be considered as a dominant process for emission of grains. Ragweed rarely exceeds 1 to 2 m above the ground, where the wind speed is moderate. In this case, the dominant
5   factor could be the temperature, considering the grains are emitted under highest temperature when they are sufficiently dry (Holmes and Bassett, 1963). The precipitation rate is a limiting factor but not the most important one: even if it rains during the night, the grains can dry out and can be pulled off the plant in the morning. R_{TS} is thus estimated as:

$$R_{TS} = \frac{\dfrac{T_{2m}}{T_{2m,0}} \times \dfrac{w_*}{w_{*,0}} \times \dfrac{SW_d}{SW_{d,0}}}{r_{q_{2m}} + r_{Pr}} \tag{57}$$

where the values of T_{2m}, w_* and SW_d correspond to the mean daily value. These values are normalized in order to keep the
10   release term nondimensional. The normalization factors are $T_{2m,0}$=10°C, $w_{*,0}$=1 m.s^{-1} and $SW_{d,0}$=200 W.m^{-2}.

In order to moderate these fluxes when meteorological conditions are not favorable, resistance terms are added. These resistances are mainly due to the 2 m specific humidity q_{2m} and the precipitation rate Pr. Each resistance is expressed as a sigmoid function ranging between 0 and 1, depending on minimal and maximal value of the x parameter. The resistance has to reflect the fact that these parameters inhibit ragweed pollen emissions.

$$15 \quad r_x = 1 + exp\left[\frac{-b_f(i_{max} - i_{min})}{2}\left(\frac{x}{x_{max} - x_{min}} - 1\right)\right] \tag{58}$$

with b_f being a constant chosen here as b_f=10, that determines the curve of the sigmoid function. i_{min} and i_{max} represent the range of the sigmoid and are here chosen as i_{min}=0 and i_{max}=1 in order to use a normalized function for each resistance. The critical issue here is to choose the minimum and maximum value for each x meteorological parameter. These boundaries have to reflect the best possible range of variations of meteorological variables, for all locations over Europe and for the whole
20   year. The maximum values must be moderate enough in order to provide a realistic resistance: a too low maximum value would give a resistance of 1 too often, while a too high maximum value would give too low resistances. Based on all meteorological values used in this study, the boundaries for the 2m specific humidity are $q_{2m}(min)$=0 and $q_{2m}(max)$=5.10^{-3} g g^{-1} and for the precipitation rate are $Pr(min)$=0 and $Pr(max)$=1.5 mm h^{-1}.

6.3   Changes in mineral dust emission

25   Two main novelties were developed in this model version. First, the way to calculate the fluxes is now following a subgrid scale variability, blending the percentages of soil in each percentage of landuse and the Weibull distribution for the surface wind speed. It enables to calculate a flux whatever the horizontal resolution and as if it was at high resolution. Second, a link was added between vegetation fires emissions and mineral dust emissions (user's choice). We consider that vegetation fires are

changing the soil and landuse properties then create more erodible surfaces. In addition and during the fire, a vertical injection
30   profile is applied to dust emission, considering that the fires induces a local convection.

6.3.1   Subgrid scale variability of the soil and landuse

The principle of the calculation of emission flux was reshaped to be more efficient. The principle of subgrid scale variability is used. The main goal is to remove, as far as possible, the problem associated with the horizontal resolution when using emission schemes based on threshold calculation principle. Thus, emission fluxes are calculated at the highest possible resolution then summed up in the grid cell. For that, the input databases are pre-processed to have subgrid tables, as presented in Figure 4. In

5   this Figure, the big square represents a CHIMERE grid cell (here for example with a size of 8 km, with each sub square with a resolution of 1 km). For each grid cell, we count the number of different landuse classes and the number of different soil types. It defines a table being a matrix and containing the relative part of each landuse classes in each soil type. For each value, we also attache the value of the saltation roughness length, z_0 and the MODIS erodibility, also with a 1 km resolution. After calculation of all values, the table is sorted as a function of the landuse for each soil. Later, in CHIMERE, the sorted table

10   enables to optimize the calculation speed by exiting the loop when the landuse relative part becomes zero.
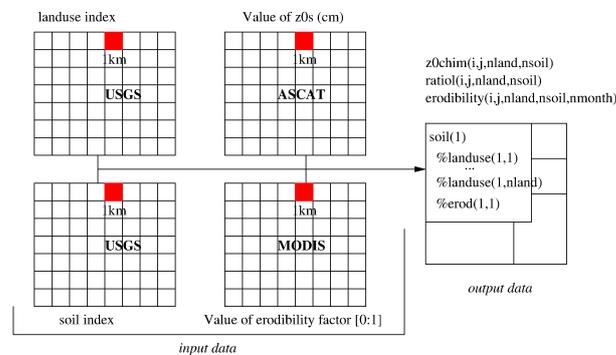
Figure 4. *The three datasets (kilometric resolution) are read together to build sub-grid scale variability tables. For each cell, the relative percentage of landuse for each soil type is calculated (ratiol), as well as the corresponding aeolian roughness length (z0chim).*

The interest is that we can calculate mineral dust flux using threshold parameters such as aeolian roughness length, as if we had a 1km × 1km horizontal resolution. With the sorted table, the calculation is fast. The weakness is that with this subgrid scale approach, we lost the spatial position of the high resolution: we know there is n% of a landuse but we don't know where in the grid cell. Note it is not very important, because we use the mean wind speed for the emissions calculation. For each

15   subgrid part, the emission flux calculation is done by iterating on the Weibull distribution.

6.3.2 Impact of the fires on dust

Vegetation fires may have an impact on mineral dust emission by changing the soil and landuse characteristics as well as the surface wind speed. A link is added between the vegetation fires emission and the mineral dust emission (Menut et al., 2022) depending if *ifire2lai* flag is activated or not. This link is only valid using the CAMS vegetation fires emissions, because some specific information (such as the burnt area surface) are needed and only the CAMSfires program, distributed with CHIMERE, has received this development. The fires have several impacts. First, short terms impacts are modelled and active only during the fire (i) the local pyroconvection create a surface pressure gradient then increases the surface wind speed, (ii) the pyroconvection induces a local thermal, quickly mixing the surface emission in the whole atmospheric column. It has the effect to increase the surface emissions and then transport these emissions vertically, when usual emission model only distributes fluxes into the first vertical model level. Second, long term effects are also parameterized: burning the surface, vegetation fires create additional barren surfaces, with more erodible properties for the mineral dust emissions.

7 Changes in deposition and chemistry

7.1 The settling velocity

The calculation of the settling velocity for aerosols has been updated using the AerSett v1 formulation (Mailler et al., 2023a). As described in Mailler et al. (2023b), the terminal fall speed of aerosols is calculated as:

$$\widetilde{v}_\infty^{Stokes} = C_c \frac{D^2 \left(\rho_p - \rho_a\right) g}{18\mu} \; ; \tag{59}$$

$$\widetilde{R} = \frac{\rho_a D \widetilde{v}_\infty^{Stokes}}{2\mu} \; ; \tag{60}$$

$$v_\infty = \widetilde{v}_\infty^{Stokes} \times \left[1 - \left(1 + \left(\frac{\widetilde{R}}{2.440} \right)^{-0.4335} \right)^{-1.905} \right] \tag{61}$$

In Eq. 59, the slip-correction factor C_c is obtained following the classical Davies (1945) formulation (where $Kn = \frac{2\lambda}{D}$ is the Knudsen number, D being the particle diameter and λ the mean free path of molecules in air:

$$C_c = 1 + Kn \left(1.257 + 0.4 \exp \left(-\frac{1.1}{Kn} \right) \right) . \tag{62}$$

As discussed in Mailler et al. (2023b), the value of v_∞ obtained from Eq. 61 stays always within 2% of the "theoretical" v_∞ value obtained from the Clift and Gauvin (1971) parameterization, but is 4 times as fast as a brute-force iterative calculation of v_∞. For small particles ($\widetilde{R} < 0.116$), Eq. 61 is replaced by just $v_\infty = \widetilde{v}_\infty^{Stokes}$, changing the result by less than 1%. This typically applies to all particles with $D < 10\,\mu$m, while for large particles Eq. 61 takes into account the Clift and Gauvin (1971) large-particle drag correction factor.

7.2 Impact of fires on dry deposition

A new process was added in the model. The dry deposition fluxes depends on the Leaf Area Index for the calculation of the surface resistance r_c (Simpson et al., 2012). More precisely, the bulk canopy resistance is expressed as:

$$G_c = LAI \times g_{sto} + G_{ns} \tag{63}$$

where LAI is the Leaf Area Index (in m^2.m^{-2}), g_{sto} the stomatal conductance, G_{ns} the bulk non-stomatal conductance.

In case of using fires emissions (user's choice), we consider a new impact in this model version: the fires destroy the vegetation and modify the soil properties (a soil dryer and more erodible). It has an impact on the mineral dust emissions (as described in Section 6.3.2), but also on the vegetation, then the LAI. The effect of the fires is cumulated in time, for the moment from the beginning of each year. For the LAI, its decrease due to the fires is expressed as:

$$LAI = LAI \times \frac{S_{total} - S_{burnt}}{S_{total}} \tag{64}$$

where S_{total} is the total surface of the grid cell when a fire is active or was previously diagnosed. S_{burnt} is the time-cumulated burnt surface.

7.3 Update the ISORROPIA module

The ISORROPIA module has been used for a long time in the model in order to simulate the partitioning of inorganic aerosols, (Nenes et al., 1998). This module is written originally in FORTRAN77 and is used in both its forward and reverse modes in CHIMERE. In order to solve possible instability issues as well as increase the readability of the module, we opted in using a Fortran90 version of ISORROPIA.

This was partially done by adapting the ISORROPIA module used in the GEOS-Chem (Horowitz, 2023) model for CHIMERE. Since GEOS-Chem only uses the forward mode of ISORROPIA, we opted in adding the reverse mode into the module. The entirely translated version was then tested both outside (as in in a 0D configuration) and inside CHIMERE. It was concluded that the two modules provide the same results while the Fortran90 version of the module is more stable than the FORTRAN77 version. This stable version is now part of the CHIMERE model.

8 Model validation

8.1 Simulation and validation set-up

The model goes through continuous quality control validations. Six simulations are designed. First, with two model versions, (i) with the previous model version v2020r3, (ii) with this new version v2023r1. Second, for each version, with three different configurations: (i) in offline mode and forced by ECMWF meteorological fields, (ii) in offline mode and forced by WRF 4.3,

(iii) in online mode, also with WRF 4.3. These three configurations are chosen since they show the results of the model with
30 two major meteorological forcings as well as the effect of coupling with an online meteorological model on the simulated concentrations.

The simulations are performed over a domain that covers most of Europe and Northern Africa. This domain is usually used for validation purposes since it takes into account a region containing all the possible emission sources in the model i.e. anthropogenic, biogenic, biomass burning, sea-salt, and dust sources. The horizontal resolution of the model is 60×60 km. Vertical resolution of the model has 15 levels, starting from surface and going up to 300 hPa. The simulations are performed 5 for the entire year of 2019 in order to take into account seasonal changes. For simulations using WRF, this model is forced by the CFSv2 meteorological inputs (Saha et al., 2011); for simulations using ECMWF the meteorology from the IFS/ECMWF fields, with a 0.25×0.25 degrees global resolution and 3-hourly time frequency are used. Anthropogenic emissions come from the CAMS global emission inventory (v5.3, Soulie et al. (2023)). Mineral dust, salt, DMS, anthropogenic, biogenic and NO_x from lightening emissions have all been calculated. The CAMS global reanalysis 6-hourly fields are used as initial/boundary 10 conditions. The CHIMERE model is run with 10 aerosol size bins starting from 10 nm and going up to 40 μm.

For the calculation of statistical scores, the EvalTools module is used. It is a python package developed by INERIS and Meteo-France and freely available on a web site (*https://opensource.umr-cnrm.fr/projects/evaltools*, version 1.0.6r). Being also used by INERIS in the framework of the daily operational forecast using CHIMERE over France (PREV'AIR) and Europe (CAMS Copernicus), the advantage to use this tool is to be completely homogeneous with the validation made for the 15 operational forecast.

Measurements used for these comparisons are collected from multiple sources. The model is validated on a regular basis with a vast amount of data for a large list of species downloaded from several sources. Starting with the meteorological data, 2m temperature, wind speed, precipitation and relative humidity are compared. These measurements come from E-OBS, the British Atmospheric Data Centre network (BADC, http://data.ceda.ac.uk/badc, last access: 6 December2023) and EBAS 20 (https://ebas-data.nilu.no/, last access: 6 December 2023). The E-OBS dataset (prepared by the ECA&D project) provides daily data on a regular 0.1×0.25 grid covering the European area. For all variables provided by E-OBS data for the EEA ozone (O_3) stations are extracted from the gridded format and compared to the simulations.

For atmospheric pollutants, a long list of species is compared to the simulations on a regular basis, but only certain comparisons will be presented in this paper. Ground-level measurements of O_3, PM_{10} and $PM_{2.5}$ are downloaded from the European Environment Agency (EEA, https://www.eea.europa.eu, last access: 6 December 2023), EBAS and OPENAQ (https://openaq.org/, last access: 6 December 2023). The observations for aerosol optical depth (AOD) downloaded from the Aerosol RObotic NETwork global remote sensing network (AERONET, https://aeronet.gsfc.nasa.gov/, last access: 6 December 5 2023) are also included.

The comparisons have been performed for all types of stations. It should be noted that all the data mentioned here are on an hourly resolution, apart from the E-OBS data. Only stations with at least 90% data availability threshold for the entire year of 2019 have been used. An exception has been given to the AOD data, where the data availability during the year as been fixed at 25%. The number of stations used for each of these sources is given in table Table 7.

10 We have also included validation for vertical profiles of pressure, temperature, and O_3 using the data acquired from the World Ozone and Ultraviolet Radiation Data Centre (WOUDC, https://woudc.org/home.php, last access: 6 December 2023) resulting from ozonesonde measurements. There are 700 balloon flights inside the simulation domain having sufficient data during the year from 9 locations. Only stations with over 25 flights during the year were used for the comparisons.

	T2m	WS	P	rH	O_3	PM_{10}	$PM_{2.5}$	AOD
EEA	-	-	-	-	1745	27	17	-
EBAS	27	22		27	111	1242	627	-
OPENAQ	-	-	-	-	232	241	233	-
E-OBS	3110	3110	3110	3110	-	-	-	-
BADC	1234	1157	1606		-	-	-	-
AERONET	-	-	-	-	-	-	-	117

Table 7. *Number of stations for all data sources per species.*

8.2 Statistical scores

15 Statistical scores are presented for O_3, $PM_{2.5}$ and PM_{10} surface concentrations and Aerosol Optical depth (AOD). The scores are calculated for six model configurations: the previous model version v2020r3, the new model version v2023r1, with three different meteorological forcings: ECMWF in offline mode, called *offecm* and WRF in offline and online modes, respectively called *offwrf* and *onwrf*.

Results for ozone surface concentrations are presented in Figure 5. On the top of the figure, the hourly mean bias is presented for the six simulations, with the three v2020r3 configurations on the left and the three v2023r1 configurations on the right. For each, results are calculated for the three datasets (EBAS, EEA and OpenAQ). With the old version, the bias is large and negative when comparing to EBAS, but close to zero when comparing to EEA and OpenAQ. With the new version, the bias

5 becomes low for EBAS and positive and much larger for EEA and OpenAQ. It means that independently of the surface dataset, and independently of the offline or online mode, the new version simulates more hourly ozone than the previous one. This difference may reach +12.19 and +10.4 μg. m^{-3} when v2023r1_onwrf simulations are compared to EEA and OpenAQ, respectively. It means that compared to the previous version, there is a positive shift of about $\approx$ +9/+10 μg. m^{-3} for the surface ozone concentrations.

10 For the correlation, bottom of Figure 5, the values show an increase from the old model version to the new one. For example, for *onwrf*, correlation increases from 0.55 to 0.65 with EBAS, from 0.61 to 0.70 with EEA and from 0.63 to 0.71 with OpenAQ. This increase is noted for the three model configurations, with or without direct/indirect effects. In average, the new model version provides correlation with an increase of +0.07 for ozone.

Figure 6 presents the same kind of validation but for PM_{10} surface concentrations. The mean bias is reduced for all simula-

15 tions and changes from largely negative to slightly positive. For example and for the online coupling, the bias of -8.08 and -9.89
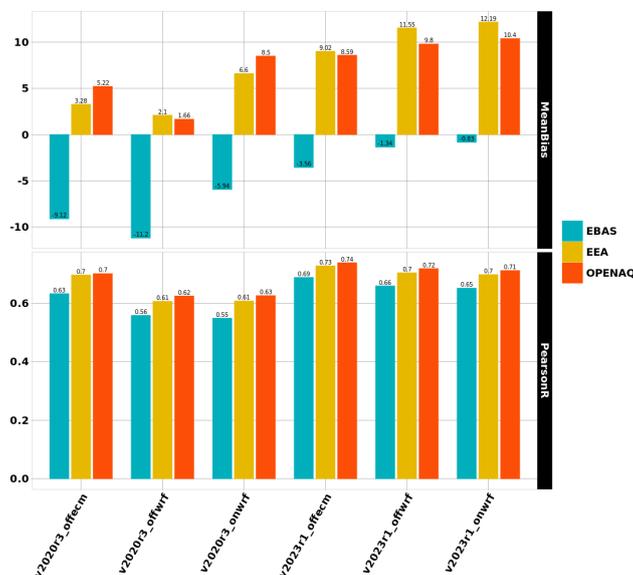
Figure 5. *Statistical scores for ozone.*

μg.m^{-3} for the comparison to EEA and OpenAQ changes to -2.18 and -2.71 μg.m^{-3} with the v2023r1 model version. On the other hand, and by comparison to EBAS data, the bias changed from 0.35 to 4.6 μg.m^{-3}. In average the surface concentrations of PM$_{10}$ increase in average by $\approx$ 5 μg.m^{-3} for all model configurations of v2023r1 compared to v2020r3. As for ozone, the correlation systematically increases with the new model version. If we consider the validation by comparison to EEA data, we can see an increase from 0.46 to 0.50 when the meteorological forcing is *offecm*. The increase is much larger when the meteorological forcing is the WRF model, with for example for *onwrf* a increase from 0.26 to 0.44 from the old to the new

5 model version. In average, the gain in correlation is roughly +0.05 when the forcing is *offecm* and +0.2 when the forcing is *offwrf* or *onwrf*.

The same kind of validation is performed for Aerosol Optical Depth and results are presented in Figure 7. The only dataset is here AERONET, providing a large geographical cover of the AOD. Regarding the bias, it is slightly reduce from the old to the new model version, but the differences old/new version are very low. The bias was also smaller when using *offwrf* and *onwrf* in

10 place of *offecm*. This result remains the same with the new model version. The correlation changes with the new version. With *offecm*, one can note an increase from 0.55 to 0.59. With *offwrf* and *onwrf*, the increase is much larger with values from 0.33 and 0.32 for v2020r3 to 0.64 and 0.64 for v2023r1. Depending on the meteorological forcing the net gain on AOD correlation ranges from +0.05 to +0.3. The use of the new version is always a gain.

Another way to validate the simulations with the new model version is to compare model outputs to vertical soundings.

15 Results are synthetized in Figure 8 for ozone. All soundings recorded during the simulation period (one year) and over the whole domain are aggregated to calculate bias and correlation. Values are presented on the vertical model levels. The values
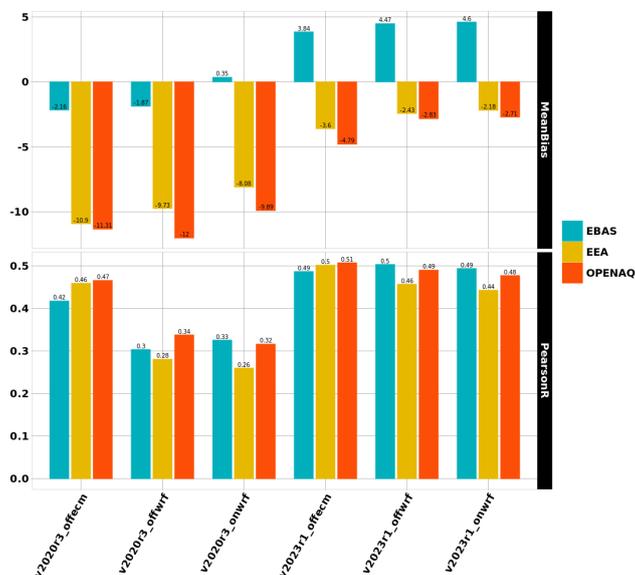
Figure 6. *Statistical scores for PM$_{10}$.*
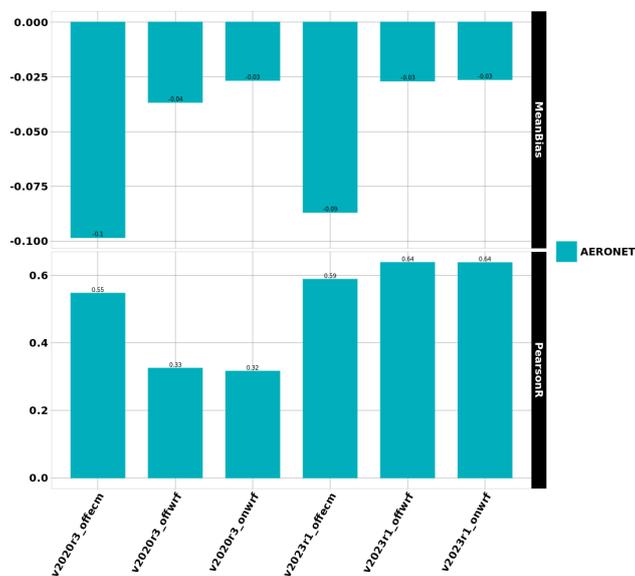
Figure 7. *Statistical scores for AOD.*

for observations are thus presented as the mean averaged (the black bar and dot) and the standard deviation as a black dot in a colored bar. At each level, the correlation is presented as colored text: the colour corresponds to the model configuration with

the best correlation. It enables to easily visualize where model configurations outperform. For this simulation, the best scores are obtained with the v2023r1 forced offline with WRF close to the surface, then with the offile ECMWF version for the rest

5   of the tropospheric column (except two model levels, where the best score is obtained the v2020r3 version). Globally, the best scores are with the v2023r1, in configuration forced by ECMWF. It is also noticeable than the standard deviation at each model level has very close values between observations and model. It is changing only close to the top where the model variability becomes larger than the observations. At these levels, the boundary conditions play a role in this variability.
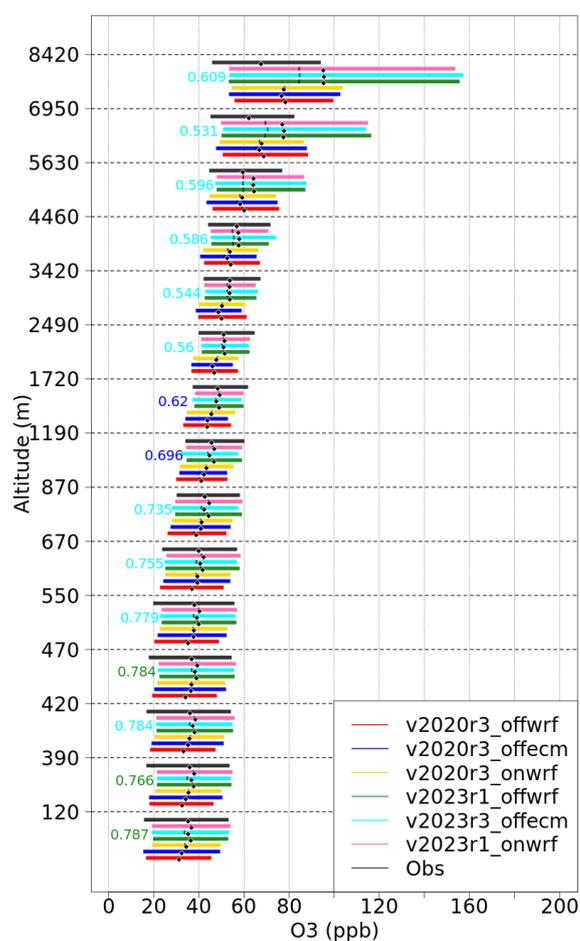
Figure 8. *Comparison between observations and model results as a mean averaged vertical profile of ozone (ppb). The data are averaged over the whole modelled period and for all available vertical soundings recorded over Europe.*

9 Conclusions

The new CHIMERE version called v2023r1 was presented in this article. It contains both new processes and new numerical
tools. More precisely for the researchers, the pollen emissions are now distributed and can be used for any local studies in
Europe, the turbulence and the transport were updated with more recent parameterizations and the impact of the fires on the
surface was added. For the users performing long simulations or forecast, the integration of the XIOS model enables to have
a faster model, with a computational cost 40% less than the previous version. It is also possible to easily manage the output,
including the possibility to write sub-hourly fields such as the maximum of concentration during an hour.

The perspectives for the model are to continue to modularize the code and to optimize the calculation. The future of such kind
of model being to go toward HPC architecture, it is important to follow the fast evolution in numerics methodology including
optimization. The use of XIOS for reading input data will also be implemented to allow some on-the-fly interpolation in case
of complex grids.

Code availability. The CHIMERE v2023 model is available on its dedicated web site https://www.lmd.polytechnique.fr/chimere. The model
sources have the DOI number https://doi.org/10.14768/7aae366b-662c-4889-900f-2d2a6101ec35.

Data availability. All data used in this study, as well as the data required to run the simulations, are available on the CHIMERE web site
https://www.lmd.polytechnique.fr/chimere.

Author contributions. All authors contributed to the model development. LM coordinated the manuscript and all authors wrote a part and
reviewed it.

Competing interests. The authors declare that they have no conflict of interest.

Acknowledgements. The authors acknowledge the OASIS modeling team for their support with the OASIS coupler, the WRF developers
team for the free use of their model and Bertrand Bessagnet for continuous discussions about aerosols modelling. They also thank the
investigators and staff who maintain and provide the AERONET data (https://aeronet.gsfc.nasa.gov/). European Environmental Agency
(EEA) is acknowledged for their air quality station data that is provided and freely downloadable (https://www.eea.europa.eu/data-and-
maps/data/aqereporting-8).

Appendix A: Tabulated roughness length and albedo

#	Landuse	$z_{0,min}$ (m)	$z_{0,max}$ (m)	#	Landuse	$z_{0,min}$ (m)	$z_{0,max}$ (m)
1	urban and built-up land	0.50	0.50	15	mixed forest	0.20	0.50
2	dryland cropland and pasture	0.05	0.15	16	water bodies	0.0001	0.0001
3	irrigated cropland and pasture	0.02	0.10	17	herbaceous wetland	0.20	0.20
4	mixed of (2) and (3)	0.05	0.15	18	wooded wetland	0.40	0.40
5	cropland/grassland mosaic	0.05	0.14	19	barren	0.01	0.01
6	cropland/woodland mosaic	0.20	0.20	20	herbaceous tundra	0.10	0.10
7	grassland	0.10	0.12	21	wooded tundra	0.30	0.30
8	shrubland	0.01	0.05	22	mixed tundra	0.15	0.15
9	mixed shrubland/grassland	0.01	0.06	23	bare ground tundra	0.05	0.10
10	savanna	0.15	0.15	24	snow or ice	0.001	0.001
11	deciduous broadleaf forest	0.50	0.50	25	playa	0.01	0.01
12	deciduous needleleaf forest	0.50	0.50	26	lava	0.15	0.15
13	evergreen broadleaf forest	0.50	0.50	27	white sand	0.01	0.01
14	evergreen needleleaf forest	0.50	0.50	28	ocean	0.0	0.0

Table A1. *USGS landuse types and minimum and maximum values of momentun roughness length z_0.*

#	Landuse	bare	snow	#	Landuse	bare	snow
1	urban and built-up land	0.035	0.3	15	mixed forest	0.025	0.558
2	dryland cropland and pasture	0.035	0.376	16	water bodies	0.07	0.836
3	irrigated cropland and pasture	0.035	0.376	17	herbaceous wetland	0.04	0.720
4	mixed of (2) and (3)	0.035	0.376	18	wooded wetland	0.04	0.720
5	cropland/grassland mosaic	0.035	0.376	19	barren	0.1	0.836
6	cropland/woodland mosaic	0.035	0.376	20	herbaceous tundra	0.04	0.720
7	grassland	0.04	0.720	21	wooded tundra	0.04	0.720
8	shrubland	0.05	0.558	22	mixed tundra	0.04	0.720
9	mixed shrubland/grassland	0.05	0.558	23	bare ground tundra	0.04	0.720
10	savanna	0.04	0.720	24	snow or ice	0.1	0.836
11	deciduous broadleaf forest	0.025	0.558	25	playa	0.1	0.836
12	deciduous needleleaf forest	0.025	0.278	26	lava	0.1	0.836
13	evergreen broadleaf forest	0.025	0.558	27	white sand	0.1	0.836
14	evergreen needleleaf forest	0.025	0.278	28	ocean	0.07	0.836

Table A2. *USGS landuse types and tabulated albedos for bare and snow surfaces.*

References

Beegum, S., I.Gherboudj, N.Chaouch, F.Couvidat, L.Menut, and H.Ghedira: Simulating Aerosols over Arabian Peninsula with CHIMERE: Sensitivity to soil, surface parameters and anthropogenic emission inventories, Atmospheric Environment, 128, 185–197, https://doi.org/10.1016/j.atmosenv.2016.01.010, 2016.

Beljaars, A. C. M. and Holtslag, A. A. M.: Flux Parameterization over Land Surfaces for Atmospheric Models, Journal of Applied Meteorology, 30, 327–341, https://doi.org/10.1175/1520-0450(1991)030<0327:FPOLSF>2.0.CO;2, 1991.

Beljaars, A. C. M. and Viterbo, P.: The sensitivity of winter evaporation to the formulation of aerodynamic resistance in the ECMWF model, Boundary-Layer Meteorology, 71, 135–149, https://doi.org/10.1007/BF00709223, http://dx.doi.org/10.1007/BF00709223, 1994.

Betts, A., Hong, S., and Pan, H.: Comparison of NCEP-NCAR Realanalysis with 1987 FIFE data, Mon. Weather Rev., 124, 1480–1498, https://doi.org/10.1175/1520-0493(1996)124, 1995.

Boucher, O., Servonnat, J., Albright, A. L., Aumont, O., Balkanski, Y., Bastrikov, V., Bekki, S., Bonnet, R., Bony, S., Bopp, L., et al.: Presentation and evaluation of the IPSL-CM6A-LR climate model, Journal of Advances in Modeling Earth Systems, 12, e2019MS002 010, 2020.

Bruin, H. A. R. D. and Holtslag, A. A. M.: A Simple Parameterization of the Surface Fluxes of Sensible and Latent Heat During Daytime Compared with the Penman-Monteith Concept, Journal of Applied Meteorology and Climatology, 21, 1610 – 1621, https://doi.org/10.1175/1520-0450(1982)021<1610:ASPOTS>2.0.CO;2, 1982.

Chapman, D. S., Haynes, T., Beal, S., Essl, F., and Bullock, J. M.: Phenology predicts the native and invasive range limits of common ragweed, Global Change Biology, 20, 192–202, https://doi.org/https://doi.org/10.1111/gcb.12380, 2014.

Charnock, H.: Wind stress over a water surface, Quart J Roy Meteorol Soc, 81, 639–640, 1955.

Cheinet, S. and Teixeira, J.: A simple formulation for the eddy-diffusivity parameterization of cloud-topped boundary layers, Geophysical Research Letters, 30, https://doi.org/10.1029/2003GL017377, 2003.

Clift, R. and Gauvin, W. H.: Motion of entrained particles in gas streams, The Canadian Journal of Chemical Engineering, 49, https://doi.org/10.1002/cjce.5450490403, 1971.

Colella, P. and Woodward, P. R.: The piecewise parabolic method (PPM) for gas-dynamical simulations, Journal of Computational Physics, 11, 38–39, 1984.

Courant, R., Issacson, E., and Reees, M.: On the Solution of Nonlinear Hyperbolic Differential Equations by Finite Differences, Comm. Pure Appl. Math., 5, 243–255, 1952.

Craig, A., Valcke, S., and Coquart, L.: Development and performance of a new version of the OASIS coupler, OASIS3-MCT_3.0, Geoscientific Model Development, 10, 3297–3308, https://doi.org/10.5194/gmd-10-3297-2017, https://gmd.copernicus.org/articles/10/3297/2017/, 2017.

Crippa, M., Solazzo, E., Huang, G., Koffi, E., Muntean, M., C., S., R., F., and G., J.-M.: High resolution temporal profiles in the Emissions Database for Global Atmospheric Research., Sci Data, 7, 2020.

Davies, C. N.: Definitive equations for the fluid resistance of spheres, Proceedings of the Physical Society, 57, 259–270, https://doi.org/10.1088/0959-5309/57/4/301, 1945.

Deen, W., Hunt, L. A., and Swanton, C. J.: Photothermal time describes common ragweed (Ambrosia artemisiifolia L.) phenological development and growth, Weed Science, 46, 561–568, https://doi.org/10.1017/S0043174500091104, 1998.

Deroubaix, A., Menut, L., Flamant, C., Brito, J., Denjean, C., Dreiling, V., Fink, A., Jambert, C., Kalthoff, N., Knippertz, P., Ladkin, R., Mailler, S., Maranan, M., Pacifico, F., Piguet, B., Siour, G., and Turquety, S.: Diurnal cycle of coastal anthropogenic pollutant transport over southern West Africa during the DACCIWA campaign, Atmospheric Chemistry and Physics, 19, 473–497, https://doi.org/10.5194/acp-19-473-2019, https://acp.copernicus.org/articles/19/473/2019/, 2019.

Després, B. and Lagoutière, F.: Un schéma non linéaire anti-dissipatif pour l'équation d'advection linéaire, Comptes Rendus de l'Académie des Sciences - Series I - Mathematics, 328, 939 – 943, https://doi.org/https://doi.org/10.1016/S0764-4442(99)80301-2, 1999.

Efstathiou, C., Isukapalli, S., and Georgopoulos, P.: A mechanistic modeling system for estimating large-scale emissions and transport of pollen and co-allergens, Atmospheric Environment, 45, 2260 – 2276, https://doi.org/10.1016/j.atmosenv.2010.12.008, 2011.

Emberson, L.-D., Ashmore, M.-R., Simpson, D., Tuovinen, J.-P., and Cambridge, H.-M.: Modelling and mapping ozone deposition in Europe, Water, Air and Soil Pollution, 130, 577–582, 2001.

Fuster, B., Sanchez-Zapero, J., Camacho, F., Garcia-Santos, V., Verger, A., Lacaze, R., Weiss, M., Baret, F., and Smets, B.: Quality Assessment of PROBA-V LAI, fAPAR and fCOVER Collection 300 m Products of Copernicus Global Land Service, Remote Sensing, 12, https://doi.org/10.3390/rs12061017, https://www.mdpi.com/2072-4292/12/6/1017, 2020.

Godunov, S. K. and Bohachevsky, I.: Finite difference method for numerical computation of discontinuous solutions of the equations of fluid dynamics, Matematičeskij sbornik, 47(89), 271–306, https://hal.archives-ouvertes.fr/hal-01620642, 1959.

Grachev, A., Fairall, C., and Bradley, E.: Convective Profile Constants Revisited., Boundary-Layer Meteorology, 94, 495–515, https://doi.org/10.1023/A:1002452529672, 2000.

Guevara, M., Jorba, O., Tena, C., Denier van der Gon, H., Kuenen, J., Elguindi, N., Darras, S., Granier, C., and Pérez García-Pando, C.: Copernicus Atmosphere Monitoring Service TEMPOral profiles (CAMS-TEMPO): global and European emission temporal profile maps for atmospheric chemistry modelling, Earth System Science Data, 13, 367–404, https://doi.org/10.5194/essd-13-367-2021, https://essd.copernicus.org/articles/13/367/2021/, 2021.

Helbig, N., Vogel, B., Vogel, H., and Fiedler, F.: Numerical modelling of pollen dispersion on the regional scale, Aerobiologia, 3, 3–19, 2004.

Hersbach, H.: Sea Surface Roughness and Drag Coefficient as Functions of Neutral Wind Speed, Journal of Physical Oceanography, 41, 247–251, https://doi.org/10.1175/2010JPO4567.1, 2011.

Holmes, R. and Bassett, I.: Effect of meteorological events on ragweed pollen count, Int. J. Biometeorol., 7, 27–34, 1963.

Horowitz, H.: GEOS-Chem 13.0.2, https://zenodo.org/record/4681742#.ZBHxFdLMKjY, [Online; accessed 9-march-2023], 2023.

Jiménez, P. A., Dudhia, J., González-Rouco, J. F., Navarro, J., Montávez, J. P., and Garcia-Bustamante, E.: A Revised Scheme for the WRF Surface Layer Formulation, Monthly Weather Review, 140, 898 – 918, https://doi.org/10.1175/MWR-D-11-00056.1, 2012.

Journet, E., Balkanski, Y., and Harrison, S. P.: A new data set of soil mineralogy for dust-cycle modeling, Atmospheric Chemistry and Physics, 14, 3801–3816, https://doi.org/10.5194/acp-14-3801-2014, http://www.atmos-chem-phys.net/14/3801/2014/, 2014.

Lachatre, M., Mailler, S., Menut, L., Turquety, S., Sellitto, P., Guermazi, H., Salerno, G., Caltabiano, T., and Carboni, E.: New strategies for vertical transport in chemistry transport models: application to the case of the Mount Etna eruption on 18 March 2012 with CHIMERE v2017r4, Geoscientific Model Development, 13, 5707–5723, https://doi.org/10.5194/gmd-13-5707-2020, 2020.

Lachatre, M., Mailler, S., Menut, L., Cholakian, A., Sellitto, P., Siour, G., Guermazi, H., Salerno, G., and Giammanco, S.: Modelling SO_2 conversion into sulfates in the mid-troposphere with a 3D chemistry transport model: the case of Mount Etna's eruption on 12 April 2012, Atmospheric Chemistry and Physics, 22, 13 861–13 879, https://doi.org/10.5194/acp-22-13861-2022, https://acp.copernicus.org/articles/22/13861/2022/, 2022.

Lana, A., Bell, T. G., Simo, R., Vallina, S. M., Ballabrera-Poy, J., Kettle, A. J., Dachs, J., Bopp, L., Saltzman, E. S., Stefels, J., Johnson, J. E., and Liss, P. S.: An updated climatology of surface dimethylsulfide concentrations and emission fluxes in the global ocean, Global Biogeochemical Cycles, 25, https://doi.org/10.1029/2010GB003850, 2011.

Lapere, R., Huneeus, N., Mailler, S., Menut, L., and Couvidat, F.: Meteorological export and deposition fluxes of black carbon on glaciers of the central Chilean Andes, Atmospheric Chemistry and Physics, 23, 1749–1768, https://doi.org/10.5194/acp-23-1749-2023, 2023.

Linkosalo, T., Ranta, H., Oksanen, A., Siljamo, P., Luomajoki, A., Kukkonen, J., and Sofiev, M.: A double-threshold temperature sum model for predicting the flowering duration and relative intensity of Betula pendula and B. pubescens, Agricultural and Forest Meteorology, 150, 1579 – 1584, https://doi.org/10.1016/j.agrformet.2010.08.007, 2010.

Louis, J.: A parametric model of vertical eddy fluxes in the atmosphere, Boundary Layer Meteorology, pp. 187–202, 1979.

Mailler, S., Menut, L., Khvorostyanov, D., Valari, M., Couvidat, F., Siour, G., Turquety, S., Briant, R., Tuccella, P., Bessagnet, B., Colette, A., Létinois, L., Markakis, K., and Meleux, F.: CHIMERE-2017: from urban to hemispheric chemistry-transport modeling, Geoscientific Model Development, 10, 2397–2423, https://doi.org/10.5194/gmd-10-2397-2017, 2017.

Mailler, S., Menut, L., Cholakian, A., and Pennel, R.: AerSett, https://doi.org/10.5281/zenodo.7535115, https://doi.org/10.5281/zenodo.7535115, 2023a.

Mailler, S., Menut, L., Cholakian, A., and Pennel, R.: AerSett v1.0: A simple and straightforward model for the settling speed of big spherical atmospheric aerosol, Geoscientific Model Development, Accepted, https://doi.org/10.5194/gmd-2022-247, 2023b.

Mailler, S., Pennel, R., Menut, L., and Cholakian, A.: An improved version of the piecewise parabolic method advection scheme: description and performance assessment in a bidimensional test case with stiff chemistry in toyCTM v1.0.1, Geosci. Model Dev., 16, 7509–7526, https://doi.org/10.5194/gmd-16-7509-2023, 2023c.

Menut, L., Bessagnet, B., Khvorostyanov, D., Beekmann, M., Blond, N., Colette, A., Coll, I., Curci, G., Foret, F., Hodzic, A., Mailler, S., Meleux, F., Monge, J., Pison, I., Siour, G., Turquety, S., Valari, M., Vautard, R., and Vivanco, M.: CHIMERE 2013: a model for regional atmospheric composition modelling, Geoscientific Model Development, 6, 981–1028, https://doi.org/10.5194/gmd-6-981-2013, 2013.

Menut, L., Bessagnet, B., Briant, R., Cholakian, A., Couvidat, F., Mailler, S., Pennel, R., Siour, G., Tuccella, P., Turquety, S., and Valari, M.: The CHIMERE v2020r1 online chemistry-transport model, Geoscientific Model Development, 14, 6781–6811, https://doi.org/10.5194/gmd-14-6781-2021, 2021a.

Menut, L., Khvorostyanov, D., Couvidat, F., and Meleux, F.: Impact of Ragweed Pollen Daily Release Intensity on Long-Range Transport in Western Europe, Atmosphere, 12, https://doi.org/10.3390/atmos12060693, https://www.mdpi.com/2073-4433/12/6/693, 2021b.

Menut, L., Siour, G., Bessagnet, B., Cholakian, A., Pennel, R., and Mailler, S.: Impact of Wildfires on Mineral Dust Emissions in Europe, Journal of Geophysical Research: Atmospheres, 127, e2022JD037 395, https://doi.org/https://doi.org/10.1029/2022JD037395, https://agupubs.onlinelibrary.wiley.com/doi/abs/10.1029/2022JD037395, e2022JD037395 2022JD037395, 2022.

Menut, L., Cholakian, A., Siour, G., Lapere, R., Pennel, R., Mailler, S., and Bessagnet, B.: Impact of Landes forest fires on air quality in France during the 2022 summer, Atmospheric Chemistry and Physics, 23, 7281–7296, https://doi.org/10.5194/acp-23-7281-2023, https://acp.copernicus.org/articles/23/7281/2023/, 2023.

Nenes, A., Pilinis, C., and Pandis, S.: ISORROPIA: A new thermodynamic model for inorganic multicomponent atmospheric aerosols, Aquatic Geochem., 4, 123–152, 1998.

Paulson, C. A.: The Mathematical Representation of Wind Speed and Temperature Profiles in the Unstable Atmospheric Surface Layer, Journal of Applied Meteorology and Climatology, 9, 857 – 861, https://doi.org/10.1175/1520-0450(1970)009<0857:TMROWS>2.0.CO;2, 1970.

Pena, A. and Gryning, S.-E.: Charnock's Roughness Length Model and Non-dimensional Wind Profiles Over the Sea, Boundary-Layer Meteorology, 128, 191–203, https://doi.org/10.1007/s10546-008-9285-y, 2008.

Prank, M., Chapman, D., Bullock, J., Belmonte, J., Berger, U., Dahl, A., Jager, S., Kovtunenko, I., Magyar, D., Niemela, S., Rantio-Lehtimaki, A., Rodinkova, V., Sauliene, I., Severova, E., Sikoparija, B., and Sofiev, M.: An operational model for forecasting ragweed pollen release and dispersion in Europe, Agricultural and Forest Meteorology, 182, 43–53, 2013.

Prigent, C., Jiménez, C., and Catherinot, J.: Comparison of satellite microwave backscattering (ASCAT) and visible/near-infrared reflectances (PARASOL) for the estimation of aeolian aerodynamic roughness length in arid and semi-arid regions, Atmos. Meas. Tech., 5, 2703–2712, 2012.

Saha, S., Moorthi, S., Wu, X., Wang, J., Nadiga, S., Tripp, P., Behringer, D., Hou, Y.-T., ya Chuang, H., Iredell, M., Ek, M., Meng, J., Yang, R., Mendez, M. P., van den Dool, H., Zhang, Q., Wang, W., Chen, M., and Becker, E.: NCEP Climate Forecast System Version 2 (CFSv2) 6-hourly Products, https://doi.org/10.5065/D61C1TXF, 2011.

Sartelet, K., Couvidat, F., Wang, Z., Flageul, C., and Kim, Y.: SSH-Aerosol v1.1: A Modular Box Model to Simulate the Evolution of Primary and Secondary Aerosols, Atmosphere, 11, https://doi.org/10.3390/atmos11050525, 2020.

Schaffner, U., Steinbach, S., Sun, Y., Skjoth, C. A., de Weger, L. A., Lommen, S. T., Augustinus, B. A., Bonini, M., Karrer, G., Šikoparija, B., Thibaudon, M., and Müller-Schärer, H.: Biological weed control to relieve millions from Ambrosia allergies in Europe, Nature communications, 11, 1745, https://doi.org/10.1038/s41467-020-15586-1, 2020.

Simpson, D., Benedictow, A., Berge, H., Bergström, R., Emberson, L. D., Fagerli, H., Flechard, C. R., Hayman, G. D., Gauss, M., Jonson, J. E., Jenkin, M. E., Nyíri, A., Richter, C., Semeena, V. S., Tsyro, S., Tuovinen, J.-P., Valdebenito, A., and Wind, P.: The EMEP MSC-W chemical transport model - technical description, Atmospheric Chemistry and Physics, 12, 7825–7865, https://doi.org/10.5194/acp-12-7825-2012, http://www.atmos-chem-phys.net/12/7825/2012/, 2012.

Sindelarova, K., Granier, C., Bouarar, I., Guenther, A., Tilmes, S., Stavrakou, T., Müller, J.-F., Kuhn, U., Stefani, P., and Knorr, W.: Global data set of biogenic VOC emissions calculated by the MEGAN model over the last 30 years, Atmospheric Chemistry and Physics, 14, 9317–9341, https://doi.org/10.5194/acp-14-9317-2014, https://acp.copernicus.org/articles/14/9317/2014/, 2014.

Sofiev, M., Siljamo, P., Ranta, H., and Rantio-Lehtimaki, A.: Towards numerical forecasting of long-range air transport of birch pollen: theoretical considerations and a feasibility study, Int J Biometeorol, 50, 392–402, 2006.

Sofiev, M., Siljamo, P., Ranta, H., Linkosalo, T., Jeager, S., Rasmussen, A., Rantio-Lehtimaki, A., Severova, E., and Kukkonen, J.: A numerical model of birch pollen emission and dispersion in the atmosphere. Description of the emission module., Int. J. Biometeorol., 57, 45–58, https://doi.org/10.1007/s00484-012-0532-z, 2013.

Soulie, A., Granier, C., Darras, S., Zilbermann, N., Doumbia, T., Guevara, M., Jalkanen, J.-P., Keita, S., Liousse, C., Crippa, M., et al.: Global Anthropogenic Emissions (CAMS-GLOB-ANT) for the Copernicus Atmosphere Monitoring Service Simulations of Air Quality Forecasts and Reanalyses, Earth System Science Data Discussions, 2023, 1–45, https://doi.org/https://doi.org/10.5194/essd-2023-306, 2023.

Troen, I. and Mahrt, L.: A simple model of the atmospheric boundary layer: Sensitivity to surface evaporation, Boundary-Layer Meteorology, 37, 129–148, 1986.

Van Leer, B.: Towards the ultimate conservative difference scheme. IV. A new approach to numerical convection, Journal of Computational Physics, 23, 276 – 299, https://doi.org/https://doi.org/10.1016/0021-9991(77)90095-X, 1977.

Walcek, C. J.: Minor flux adjustment near mixing ratio extremes for simplified yet highly accurate monotonic calculation of tracer advection, J. Geophys. Res., 105, 9335–9348, https://doi.org/10.1029/1999JD901142, 2000.

XIOS: XIOS wiki page, https://forge.ipsl.jussieu.fr/ioserver, [Online; accessed 9-march-2023], 2023.

Yuan, H., Dai, Y., Xiao, Z., Ji, D., and Shangguan, W.: Reprocessing the MODIS Leaf Area Index products for land surface and climate modelling, Remote Sensing of Environment, 115, 1171–1187, https://doi.org/https://doi.org/10.1016/j.rse.2011.01.001, https://www.sciencedirect.com/science/article/pii/S0034425711000149, 2011.